

# JGR Atmospheres

## RESEARCH ARTICLE

10.1029/2021JD035079

### Key Points:

- Global nuclear war injecting 150 Tg of stratospheric smoke causes a peak global ozone loss of 75% with depletion lasting 15 years
- Ozone loss leads to a tropical ultraviolet (UV) Index above 35 after 3 years lasting 4 years, and a 20% global average UV-B increase, a hazard to life
- Including smoke decreases photolytic rates, increasing ozone loss by 15% with decreasing NO<sub>x</sub> and increasing HO<sub>x</sub> catalytic cycle losses

### Supporting Information:

Supporting Information may be found in the online version of this article.

### Correspondence to:

C. G. Bardeen,  
[bardeenc@ucar.edu](mailto:bardeenc@ucar.edu)

### Citation:

Bardeen, C. G., Kinnison, D. E., Toon, O. B., Mills, M. J., Vitt, F., Xia, L., et al. (2021). Extreme ozone loss following nuclear war results in enhanced surface ultraviolet radiation. *Journal of Geophysical Research: Atmospheres*, 126, e2021JD035079. <https://doi.org/10.1029/2021JD035079>

Received 15 APR 2021

Accepted 2 SEP 2021

### Author Contributions:

**Conceptualization:** Charles G. Bardeen, Owen B. Toon  
**Data curation:** Charles G. Bardeen  
**Formal analysis:** Charles G. Bardeen, Douglas E. Kinnison, Michael J. Mills  
**Funding acquisition:** Owen B. Toon, Alan Robock  
**Investigation:** Charles G. Bardeen  
**Methodology:** Charles G. Bardeen  
**Resources:** Owen B. Toon, Alan Robock  
**Software:** Charles G. Bardeen, Francis Vitt  
**Validation:** Charles G. Bardeen, Francis Vitt  
**Visualization:** Charles G. Bardeen

## Extreme Ozone Loss Following Nuclear War Results in Enhanced Surface Ultraviolet Radiation

Charles G. Bardeen<sup>1</sup> , Douglas E. Kinnison<sup>1</sup> , Owen B. Toon<sup>2</sup> , Michael J. Mills<sup>1</sup> , Francis Vitt<sup>1</sup> , Lili Xia<sup>3</sup> , Jonas Jägermeyr<sup>4,5,6</sup> , Nicole S. Lovenduski<sup>7</sup> , Kim J. N. Scherrer<sup>8</sup> , Margot Clyne<sup>2</sup> , and Alan Robock<sup>3</sup> 

<sup>1</sup>National Center for Atmospheric Research, Boulder, CO, USA, <sup>2</sup>Department of Atmospheric and Ocean Sciences, Laboratory for Atmospheric and Space Physics, University of Colorado, Boulder, CO, USA, <sup>3</sup>Department of Environmental Sciences, Rutgers University, New Brunswick, NJ, USA, <sup>4</sup>NASA Goddard Institute for Space Studies, New York, NY, USA, <sup>5</sup>Center for Climate Systems Research, Columbia University, New York, NY, USA, <sup>6</sup>Potsdam Institute for Climate Impact Research (PIK), Potsdam, Germany, <sup>7</sup>Department of Atmospheric and Oceanic Sciences, Institute of Arctic and Alpine Research, University of Colorado, Boulder, CO, USA, <sup>8</sup>Institut de Ciència i Tecnologia Ambientals (ICTA), Universitat Autònoma de Barcelona, Cerdanyola del Vallès, Spain

**Abstract** For the first time, we use a modern climate model with interactive chemistry including the effects of aerosols on photolysis rates to simulate the consequences of regional and global scale nuclear wars (injecting 5 and 150 Tg of soot respectively) for the ozone layer and surface ultraviolet (UV) light. For a global nuclear war, heating in the stratosphere, reduced photolysis, and an increase in catalytic loss from the HO<sub>x</sub> cycle cause a 15 year-long reduction in the ozone column, with a peak loss of 75% globally and 65% in the tropics. This is larger than predictions from the 1980s, which assumed large injections of nitrogen oxides (NO<sub>x</sub>), but did not include the effects of smoke. NO<sub>x</sub> from the fireball and the fires provide a small (5%) increase to the global average ozone loss for the first few years. Initially, soot would shield the surface from UV-B, but UV Index values would become extreme: greater than 35 in the tropics for 4 years, and greater than 45 during the summer in the southern polar regions for 3 years. For a regional war, global column ozone would be reduced by 25% with recovery taking 12 years. This is similar to previous simulations, but with a faster recovery time due to a shorter lifetime for soot in our simulations. In-line photolysis provides process specific action spectra enabling future integration with biogeochemistry models and allows output that quantifies the potential health impacts from changes in surface UV for this and other larger aerosol injections.

**Plain Language Summary** Nuclear war would result in many immediate fatalities from the blast, heat, and radiation, but smoke from fires started by these weapons could also cause climate change lasting up to 15 years threatening food production. For the first time with a modern climate model, we have simulated the effects on ozone chemistry and surface ultraviolet (UV) light caused by absorption of sunlight by smoke from a global nuclear war. This could lead to a loss of most of our protective ozone layer taking a decade to recover and resulting in several years of extremely high UV light at the surface further endangering human health and food supplies.

## 1. Introduction

It has been understood since the early days of nuclear weapons testing that nuclear detonations can initiate large-scale fires in urban and rural settings (Glasstone & Dolan, 1977; OTA, 1979; Lewis, 1979). The first estimates of the massive amount of smoke that could be generated in a global-scale nuclear war were made by Crutzen and Birks (1982), and the potential for this amount of smoke injected into the stratosphere to cause global climatic change was shown by the TTAPS study (Turco et al., 1983), where the outcome was likened to a “nuclear winter.” Subsequent simulations by scientists in both the United States and the Soviet Union confirmed these results (e.g., Aleksandrov & Stenchikov, 1983; Covey et al., 1984). More recently, these results have been reproduced with modern Earth System models by Robock, Oman, and Stenchikov (2007) and Coupe et al. (2019) showing climatic effects lasting for over a decade. Prolonged heating and self-lofting by the soot lengthens its lifetime compared to the climatic effects of sulphate from a large volcanic eruption like that of Mount Pinatubo in 1991, which lasted for about 2 years (Robock, 2002).

**Writing – original draft:** Charles G. Bardeen, Douglas E. Kinnison, Lili Xia, Nicole S. Lovenduski

**Writing – review & editing:** Charles G. Bardeen, Douglas E. Kinnison, Owen B. Toon, Michael J. Mills, Francis Vitt, Lili Xia, Jonas Jägermeyr, Nicole S. Lovenduski, Kim J. N. Scherrer, Margot Clyne, Alan Robock

Originally, it was assumed that a global scale nuclear war between the United States and the Soviet Union would involve weapons with a total yield of 5,000–10,000 Mt with individual weapons having yields up to 20 Mt (Pittock et al., 1986), where a yield of 1 Mt is the energy equivalent of a million tons of TNT. Because of a series of arms control treaties, the inventories of the US and Russia have declined since. Under the New START Treaty, the US and Russia now have a combined total of approximately 6,000 strategic weapons with a total yield of about 1,500 Mt and a maximum weapon yield of about 800 kt (Kristensen & Korda, 2020a, 2020b).

In the 1970s, it was realized that the fireball from a nuclear weapon explosion would heat the atmosphere producing nitrogen oxides ( $\text{NO}_x$ ) (Bonner, 1971) and that  $\text{NO}_x$  in the stratosphere could catalytically destroy ozone ( $\text{O}_3$ ) (Crutzen, 1970). The amount of  $\text{NO}_x$  produced and the altitude to which it is injected depends on the amount of heating in the fireball, which in turn depends on the yield of the weapon (Foley & Ruderman, 1973). Weapons over about 800 kt would have fireballs energetic enough to directly inject  $\text{NO}_x$  into the stratosphere (Chang & Wuebbles, 1984). Photochemical simulations including  $\text{NO}_x$  injections from these large inventories with high-yield weapons showed Northern Hemisphere (NH)  $\text{O}_3$  losses varying from about 5% to 60% (e.g., Chang & Wuebbles, 1984; Crutzen & Birks, 1982; Pittock et al., 1986; Turco et al., 1983). In the 1980s, it was realized that smoke from the fires could help loft fireball  $\text{NO}_x$  into the stratosphere and that heating of the stratosphere by the smoke could affect chemical reaction rates (Turco et al., 1983), but these effects were not included in those early simulations. Kao et al. (1990) demonstrated that heating of the stratosphere added to the  $\text{NO}_x$  injection would cause a much larger  $\text{O}_3$  loss than the  $\text{NO}_x$  injection alone, but they were only able to run their simulation for 20 days. Recently Mills et al. (2008, 2014) and others (Stenke et al., 2013; Wagman et al., 2020) showed large  $\text{O}_3$  loss from a regional nuclear war without including any direct injection of  $\text{NO}_x$ . The  $\text{O}_3$  loss was driven entirely by the heating of the stratosphere by the smoke and the temperature sensitivity of  $\text{O}_3$  chemical reactions.

$\text{O}_3$  in the stratosphere is a strong absorber of ultraviolet (UV) radiation, which would otherwise be harmful to life at the surface. While sunlight in the UV-C range (200–280 nm) is almost completely absorbed, sunlight in the UV-B (280–300 nm) and UV-A (320–400 nm) ranges does reach the surface. In humans, high levels of UV-B can cause sunburn, photoaging, skin cancer, and cataracts (MacKie, 2000). Photoaging is the premature aging of the skin from exposure to sunlight and can cause pigmentation spots, spider veins, loss of skin tone, and wrinkles. It is also associated with higher skin cancer risks. The World Health Organization uses the UV Index (WHO, 2002) as a metric to inform people about surface UV levels. The scale for UV Index is: low (1–2), moderate (3–5), high (6–7), very high (8–10), and extreme (11+). At the extreme level, unprotected skin can burn within minutes; however, sensitivity does depend on the individual. Some places like the Andes typically have UV Index levels that are considered extreme, but the population is mostly dark-skinned and thus not as sensitive to UV. Because of this a threshold of 16 for extreme has been recommended for this region (Para et al., 2019). At highest risk are people with skin phenotype (SPT) I and II, light skinned people who do not tan easily, residing in areas of high UV as is common in Australia (Molina et al., 2000). Melanomas are the most lethal form of skin cancer representing 4% of cases but half of all deaths, and 60%–70% of melanoma cases are thought to be triggered by UV exposure (Sample & He, 2018). Following a regional nuclear war, Mills et al. (2014) found that UV Index increases by 3–6 in the summer at mid-latitudes resulting in UV Index values of 12–21, which are above the existing scales.

Recent simulations of the climate effects of a global nuclear war between the US and Russia either did not include interactive chemistry (Robock, Oman, & Stenchikov, 2007) or did not report the  $\text{O}_3$  loss or surface UV (Coupe et al., 2019). Coupe et al. (2019) did not report their  $\text{O}_3$  loss or surface UV because the actinic fluxes used for the photochemistry did not include the attenuation by the smoke. The study in the present paper interactively calculates the actinic flux in the presence of smoke and thus fixes this problem.

In this study, we repeat previous simulations of a regional nuclear war between India and Pakistan producing 5 Tg of soot (Mills et al., 2008, 2014; Robock, Oman, Stenchikov, Toon et al., 2007; Stenke et al., 2013; Toon et al., 2019; Wagman et al., 2020) and a global nuclear war between the US and Russia producing 150 Tg of soot (Coupe et al., 2019; Robock, Oman, & Stenchikov, 2007). Our simulations are focused on the changes to  $\text{O}_3$  and surface UV using an Earth System model with interactive chemistry and a sophisticated treatment of soot particles that includes the effects of aerosols on photolysis. We include a series of sensitivity tests with varying amounts of  $\text{NO}_x$  injection, both with and without including aerosols in the calculation

of actinic flux, to better characterize the importance of smoke,  $\text{NO}_x$  and these processes on determining the effects of nuclear war on ozone.

Both of these cases were originally defined based upon older weapons inventories. The weapons inventories held by India and Pakistan have likely increased in both quantity and yield, making the 5 Tg estimate on the conservative side of what might actually occur (Toon et al., 2019). The US and Russia have decreased the number and size of their weapons, so the 150 Tg estimate is likely an overestimate for a counterforce war with targets in just those two countries, but Toon et al. (2008) estimated 180 Tg or more was possible if these countries included targets in Europe and Asia. The exact amount of soot injected depends on details of the weapons used and the specific targets, so it is highly uncertain and an area of active research. Using these previously defined cases allows us to explore the range of possible values and to more easily compare with prior results.

We compare the resulting  $\text{O}_3$  losses to those found in prior studies, perform sensitivity tests for including aerosols in photolysis and various NO emissions, and discuss the implications of the  $\text{O}_3$  and UV changes on the biota. For the first time, these simulations have an in-line calculation for the actinic flux that includes aerosols, which provides improved photolysis rates, and high spectral resolution fluxes allowing the output of spectral action functions, weighted integrals over specific wavelength ranges, for biologically important processes. Section 2 describes the model setup, Section 3 presents the results and discusses UV impacts, and Section 4 discusses the implications of these results.

## 2. Methods

### 2.1. WACCM4 Model

We use the Community Earth System Model (CESM) (Hurrell et al., 2013), a chemistry climate model with interactive atmosphere, land, ocean, and sea ice. The ocean model simulates the evolution of physical and biogeochemical parameters at  $1^\circ$  horizontal resolution with 60 vertical layers of varying depth by coupling the Parallel Ocean Program (POP) version two ocean physical model (Danabasoglu et al., 2012) with the Biogeochemical Elemental Cycling ocean biogeochemical model (Lindsay et al., 2014). The land model is the Community Land Model (CLM) version 4 with a carbon-nitrogen cycle and simulates the evolution of the land physical state, characteristics of the land surface, exchanges of energy and material with the atmosphere, and run-off into the ocean. It has a horizontal resolution of  $1.9^\circ \times 2.5^\circ$  with 15 vertical layers for the land and 10 vertical layers for lakes (Bonan et al., 2011; Oleson et al., 2010).

The atmospheric model is the Whole Atmosphere Community Climate Model version 4 (WACCM4) (Marsh et al., 2013) which has a model top around 140 km, a horizontal resolution of  $1.9^\circ \times 2.5^\circ$ , 66 vertical levels, and includes interactive chemistry. The chemistry mechanism used in this study includes a detailed representation of the middle atmosphere, with a sophisticated suite of gas-phase and heterogeneous chemistry reactions including the odd-oxygen ( $\text{O}_x$ ), odd-nitrogen ( $\text{NO}_x$ ), odd-hydrogen ( $\text{HO}_x$ ), odd-chlorine ( $\text{ClO}_x$ ), and odd-bromine ( $\text{BrO}_x$ ) reaction families. WACCM4 has been used successfully in numerous studies of stratospheric  $\text{O}_3$  chemistry (e.g., Froidevaux et al., 2019; Polvani et al., 2017; Randel et al., 2017; Solomon et al., 2015; Solomon et al., 2016; Stone et al., 2018). Vertical resolution in WACCM4 is about 1.25 km in the troposphere and stratosphere and 2.5 km in the mesosphere. To stabilize the model against the large soot perturbations, the changes described in Bardeen et al. (2017), including the addition of the Rapid Radiative Transfer Model for GCMs (RRTMG) (Iacono et al., 2000), are used for all these simulations.

All simulations are free running and external forcings, other than soot and  $\text{NO}_x$ , are configured for repeated year 2000 conditions. A control simulation was run for 19 years and each war simulation starts at year 4 of the control and lasts for 15 years allowing most simulations to return to steady state.

### 2.2. War Scenarios

In this study, two types of wars are simulated: a regional nuclear war between India and Pakistan, and a global nuclear war between the United States and Russia. The regional war follows the 5 Tg of soot scenario described in Toon et al. (2019) using 44 15 kt-weapons with urban targets in a war lasting 3 days and is similar to that used by Mills et al. (2008, 2014). Smoke is emitted instantaneously when a target is attacked.

The global war follows Coupe et al. (2019) and is similar to that used by Robock, Oman, and Stenchikov (2007). It assumes that 150 Tg of soot is emitted uniformly over the continental US and Russia. The war lasts 7 days and the smoke emissions ramp down linearly during that time. As was done in previous studies, these wars are assumed to start on May 15th of the first year. Coupe et al. (2019) and Robock, Oman, and Stenchikov (2007) did not include weapon counts or yields needed for determining  $\text{NO}_x$  emissions, so we have performed sensitivity tests with weapons inventories from: Toon et al. (2008), Kristensen and Kor-da (2020a, 2020b), and NRC (1985).

### 2.3. Soot Treatment and Emissions

Soot aerosol is treated using the Community Aerosol and Radiation Model for Atmospheres (CARMA) (Bardeen et al., 2008; Toon et al., 1988), a sectional microphysics model that allows aerosols and the processes that affect them, including coagulation and sedimentation, to be treated in a size-resolved manner. The CARMA treatment for soot follows Bardeen et al. (2017) and has been used in previous studies of smoke from nuclear war (Coupe et al., 2019; Toon et al., 2019). Rather than treating the soot as one large spherical particle of pure black carbon (BC), as is often done in aerosol models, we treat the soot as fractal particles, clusters of smaller spheres of a uniform size (monomers) whose spatial arrangement is described by its fractal properties. We assume a monomer radius of 30 nm, a fractal dimension of 2.2 and a packing coefficient of 1, which creates a particle whose overall shape is more like a sheet than a sphere. This affects the fall velocity, coagulation rate, and optical properties of the soot. The particles are emitted in a log-normal size distribution with a mean of the radius of a sphere with equivalent mass of 0.11  $\mu\text{m}$  and a width of 1.6. All soot is emitted in the vertical as a constant mixing ratio between 150 and 300 hPa.

### 2.4. $\text{NO}_x$ Emissions

$\text{NO}_x$  is a shorthand for the combination of nitric oxide (NO) and nitrogen dioxide ( $\text{NO}_2$ ). It can be created by the heat from the fireball of the nuclear explosion as well as being emitted from the surface fires cause by the explosion.  $\text{NO}_x$  in the model is emitted only as NO. There is a rapid cycling between NO and  $\text{NO}_2$  driven by  $\text{NO}_2$  photolysis during the day and rapid reformation of  $\text{NO}_2$  at night, so the choice of the  $\text{NO}_x$  species to use for emissions is not important (Brasseur & Solomon, 2005).

#### 2.4.1. Fireball $\text{NO}_x$

The amount of NO created in the fireball is proportional to the yield of the weapon. These simulations assume a rate of  $1 \times 10^{32}$  molecules of NO injected per Mt of yield (NRC, 1985). The emissions are spread uniformly between the top and bottom of the fireball. The fireball height is a function of yield determined using equations adapted from Chang et al. (1979) that fit results from Foley and Ruderman (1973):

$$Z_{\text{top}} = 21.64Y^{0.2} + (Z_{\text{trop}} - Z_{\text{ref}}) \quad (1)$$

$$Z_{\text{bot}} = 13.41Y^{0.2} + (Z_{\text{trop}} - Z_{\text{ref}}) \quad (2)$$

where  $Z_{\text{trop}}$  is the tropopause height at the target (km),  $Y$  is the yield of the weapon (Mt),  $Z_{\text{ref}}$  is a reference height of the tropopause (17 km), and  $Z_{\text{top}}$  (km) and  $Z_{\text{bot}}$  (km) are the heights of the top and bottom of the fireball. These equations have been adapted to account for the local tropopause height as the data from Foley and Ruderman (1973) were based upon atmospheric tests that were at low to mid-latitudes while a nuclear war between the US and Russia would occur mostly at mid- to high latitudes where the tropopause is lower. Fireball  $\text{NO}$  is emitted at the time of the weapon detonation. For the regional case the weapon use is spread out over 3 days (Toon et al., 2019), but for the global war case all the  $\text{NO}$  is released at the start of the war. Since we do not here have a detailed war plan for the global war case indicating when the weapons would be used, we have assumed that all the weapons are used and thus all the fireball  $\text{NO}$  is released on the first day.

#### 2.4.2. Fire $\text{NO}_x$

$\text{NO}$  can be emitted from fires as part of the combustion process. Wildfire data from Andreae (2019) are used to estimate that  $\sim 2$  g of  $\text{NO}$  is emitted per kg of fuel burned. Using the assumption of 20 g of black carbon (BC) per kg of fuel (Toon et al., 2008) that was made to determine the soot emissions for the war scenarios,

gives us a ratio of 0.1 g NO per g BC. NO is assumed to be emitted at the same location and with the same timing as the soot emissions.

### 2.5. In-Line Photolysis

In WACCM4, photolysis was previously calculated by first using a lookup table (LUT) to calculate the actinic flux in 100 wavelength bands between 121 and 750 nm and then by applying the cross-section and quantum yield for each photolysis reaction adjusted for the local temperature and pressure (Kinnison et al., 2007). Thus, the cross-sections and quantum yields were affected by heating caused by solar absorption from aerosols, but photolysis rates did not include the direct effects on actinic flux from aerosol scattering and absorption. This approach was used by Mills et al. (2008, 2014), Toon et al. (2019), and Coupe et al. (2019). For this study we added the Tropospheric Ultraviolet and Visible (TUV) model (Madronich & Flocke, 1997) version 4.2 to provide an in-line calculation of the actinic flux.

The calculation of the photolysis coefficients is divided into two regions: (a) 120–200 nm (33 wavelength intervals); and (b) 200–750 nm (67 wavelength intervals). In the older calculation, the total photolytic rate constant for each absorbing species was derived during model execution by integrating the product of the wavelength dependent top of the atmosphere flux; the atmospheric transmission function (or normalized actinic flux), the molecular absorption cross-section, and the quantum yield. The top of the atmosphere flux over these wavelength intervals can be specified from observations and varied over the 11-year solar sunspot cycle. The wavelength-dependent transmission function was derived as a function of the model abundance of O<sub>3</sub> and molecular oxygen. For wavelengths beyond 200 nm a flux LUT approach was used, based on the 4-stream off-line version of TUV. The transmission function was interpolated from the LUT as a function of altitude, column O<sub>3</sub>, surface albedo, and zenith angle. The LUT assumed a mid-latitude O<sub>3</sub> profile and scaled the result based upon the total column O<sub>3</sub>. This older approach did not include the effects of aerosols or sulfur dioxide (SO<sub>2</sub>).

The temperature and pressure dependences of the molecular cross sections and quantum yields for each photolytic process were also represented by another LUT in these wavelength regions. At wavelengths less than 200 nm, the wavelength-dependent cross section and quantum yields for each species are specified and the transmission function is calculated explicitly for each wavelength interval. There are two exceptions to this approach. In the case of the photolysis rates for NO and molecular oxygen (O<sub>2</sub>), detailed photolysis parameterizations are included in-line. In the Schumann-Runge band region, the parameterization of NO photolysis in the δ-bands is based on Minschwaner and Siskind (1993). This parameterization includes the effect of self-absorption and subsequent attenuation of atmospheric transmission by the model-derived NO concentration. For O<sub>2</sub> photolysis, the Schumann-Runge band and Lyman-alpha parameterizations are based on Koppers and Murtagh (1996) and Chabrilat and Kockarts (1997, 1998), respectively.

For the current study we added the TUV model to provide an in-line calculation of the actinic flux. The in-line version differs from the LUT approach discussed above in that a 2-stream version of TUV is used for computational efficiency. For consistency with prior work, the same band structure, cross-sections, and quantum yields are used. Using in-line TUV allows the actual O<sub>3</sub>, SO<sub>2</sub>, and aerosol profiles in the column to be included in the calculation. For the aerosols, the optical properties calculated for the coarser band structure used by the radiative transfer code have been interpolated onto the wavelength grid used by TUV. TUV is also able to output spectral integrals of useful radiative fluxes and biologically important action spectra such as UV-B and photosynthetically available radiation (PAR, 400–700 nm) that can aid in understanding the effects on the biota of the changes to O<sub>3</sub> and to the aerosols.

## 3. Results and Discussion

We first describe changes to O<sub>3</sub> and surface UV from a regional nuclear war compared to results from Mills et al. (2008, 2014) and then evaluate O<sub>3</sub> depletion following a global nuclear war compared to results from the 1980s (Kao et al., 1990; Pittcock et al., 1986). All the WACCM4 simulations made for this study are summarized in Table 1. The notation has the name of the potential conflict (e.g., IP is India-Pakistan) and the base cases include TUV with aerosols affecting photolysis and NO emission from the fireball and the fires. A minus sign (–) indicates that a process is not included (e.g., IP–AOD means the India-Pakistan case, but

**Table 1**

List of the Whole Atmosphere Community Climate Model Version 4 / Community Aerosol and Radiation Model for Atmospheres(WACCM4/CARMA) Simulations Performed in This Study and our Prior Work

Case	Soot	NO	TUV	AOD	Yields (Mt)
Control	0 Tg	0 Tg	X	X	None
Toon et al. (2019)	5 Tg	0 Tg			Total: 0.66 Mt ( $44 \times 0.015$ )
IP	5 Tg	0.5 Tg	X	X	Same as above
IP-AOD	5 Tg	0.5 Tg	X	X	Same as above
IP-NO	5 Tg	0 Tg	X	X	Same as above
Coupe et al. (2019)	150 Tg	0 Tg			None
UR	150 Tg	22.5 Tg	X	X	Total: 1,494 Mt (R: $48 \times 0.05$ , $1232 \times 0.1$ , $580 \times 0.25$ , $574 \times 0.8$ ; US: $1486 \times 0.09$ , $528 \times 0.15$ , $200 \times 0.3$ , $600 \times 0.335$ , $322 \times 0.36$ , $384 \times 0.455$ ) Kristensen and Korda (2020a, 2020b)
UR-AOD	150 Tg	22.5 Tg	X		Same as above
UR-NO	150 Tg	0 Tg	X	X	None
UR+NO2	150 Tg	21.6 Tg	X	X	Total: 1,320 Mt ( $4400 \times 0.3$ ) Toon et al. (2008) (0.1 Mt $\rightarrow$ 0.3 Mt)
UR+NO3	150 Tg	39.9 Tg	X	X	Total: 5,000 Mt ( $220 \times 1.5$ , $2200 \times 1.0$ , $330 \times 0.75$ , $1600 \times 0.5$ , $2400 \times 0.25$ , $3200 \times 0.1$ , $12500 \times 0.04$ ) NRC (1985) (no ground bursts)

Note. IP indicates a regional conflict between India and Pakistan, and UR indicates a global conflict between the US and Russia. Soot shows the total soot emission, NO the total NO emission (fireball and fire), TUV indicates that in-line TUV was used for photolysis, and AOD indicates that the aerosol optical depth was included in the TUV photolysis calculation. Yields indicate the total yield, the count and size (Mt) of the individual weapons that are assumed for the NOx production, and the source of the weapon inventory. For Toon et al. (2008), the weapon yield was assumed to be 300 kt rather than 100 kt. For NRC (1985), 1,500 Mt of ground bursts were not included in the total. The different NO emission cases (NO, NO2, and NO3) are sensitivity tests that differ only in the amount and altitude extent of the fireball NO emission.

not accounting for the effects of aerosols, using AOD to mean aerosol optical depth, in the chemistry calculations) and a plus sign (+) indicates that alternate fireball NO emissions were used. Climate effects other than those related to O<sub>3</sub> and surface UV have already been described in Coupe et al. (2019) for the global war case and Toon et al. (2019) for several regional war cases. Our climate results are similar to these and thus will not be discussed here; however, we do show the evolution of the global (Figures 1 and S1) and polar

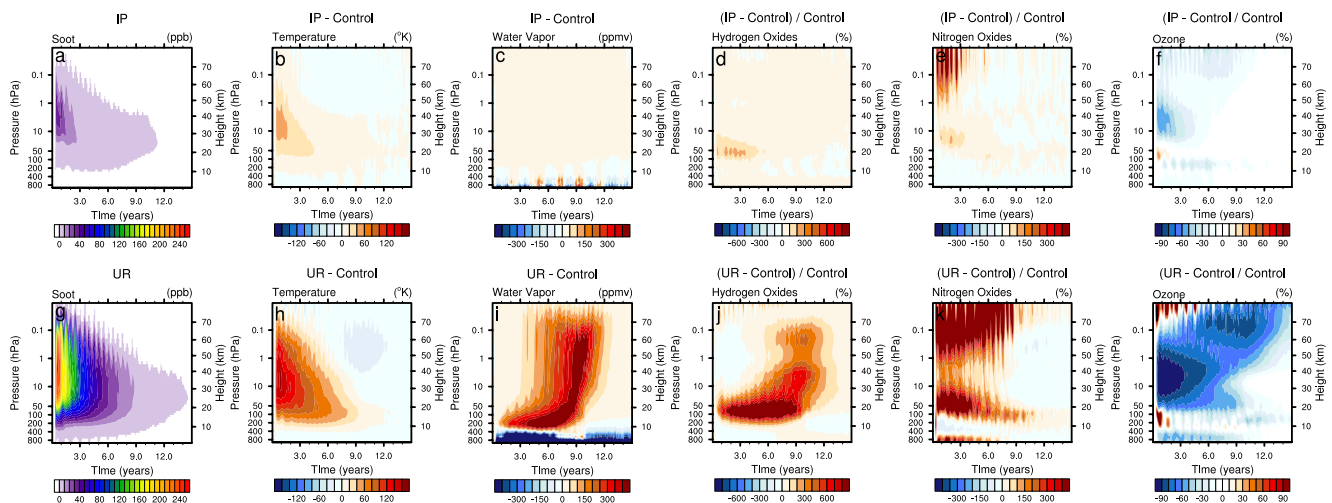


**Figure 1.** Evolution of the change in the global average vertical profile for soot (a), (g), temperature (b), (h), H<sub>2</sub>O (c), (i), HO<sub>x</sub> (d), (j), NO<sub>x</sub> (e), (k), and O<sub>3</sub> (f, l) for the India-Pakistan (IP) (top) and UR (bottom) cases from the control. Soot, temperature, and H<sub>2</sub>O are shown as differences, while HO<sub>x</sub>, NO<sub>x</sub>, and O<sub>3</sub> are shown as percentage differences. Scales are the same for the IP and UR cases. HO<sub>x</sub> is the sum of H, OH, and HO<sub>2</sub>, and NO<sub>x</sub> is the sum of N, NO, and NO<sub>2</sub>.

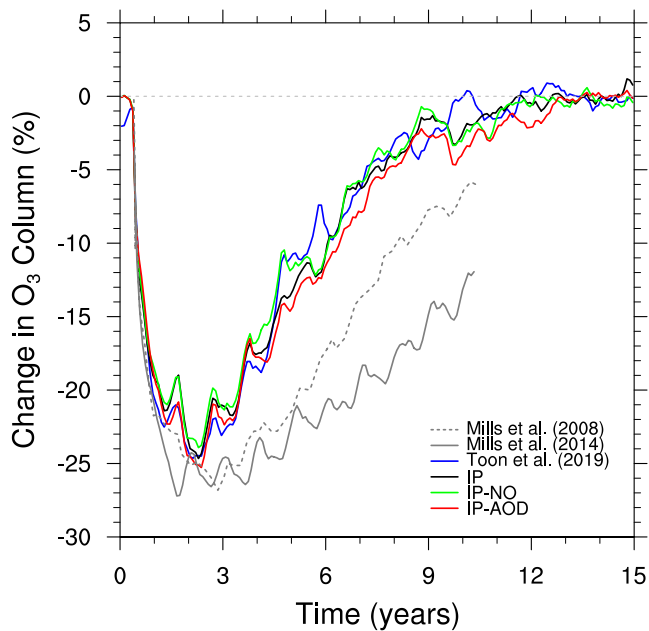


**Figure 2.** Evolution of the change in global average column  $O_3$  for the 5 Tg soot injection regional nuclear war cases: Mills et al. (2008), Mills et al. (2014), Toon et al. (2019), India-Pakistan (IP), IP-NO, and IP-AOD. See Table 1 for the abbreviations and descriptions of the IP cases from this study.

(Figures S2 and S3) average vertical profile changes for soot, temperature,  $H_2O$ ,  $HO_x$ ,  $NO_x$ , and  $O_3$  from our regional and global war cases.

### 3.1. Regional Nuclear War

Mills et al. (2008, 2014) assumed that a nuclear conflict involving India and Pakistan generated 5 Tg of soot with the soot spread uniformly over the region. Mills et al. (2008) used WACCM3 and Mills et al. (2014) used WACCM4 with a fixed size of 100 nm for the soot to simulate the resulting climate effects. Toon et al. (2019) recreated a similar case; however, they used emissions from a specific set of targets and weapon yields, a fractal representation for the soot, and the soot was allowed to coagulate. This study repeats Toon et al. (2019) but includes in-line photolysis from TUV as well as  $NO_x$  emissions from the fireballs and the fires. Figure 2 shows the evolution of the change in the monthly global average  $O_3$  column for several cases compared to their control cases. All these cases show a peak  $O_3$  loss of  $\sim 25\%$  2–3 years after the war, but the fractal soot cases (IP, IP-NO, IP-AOD, and Toon et al., (2019)) all show a faster recovery of 12 years than Mills et al. (2008, 2014), because the soot particles grow larger ( $>500$  nm) and thus have a shorter lifetime in the stratosphere. Mills et al. (2008) showed faster  $O_3$  recovery than that in Mills et al. (2014) because Mills et al. (2008) used specified sea surface temperatures and had a horizontal resolution of  $4^\circ$  latitude by  $5^\circ$  longitude, which led to a faster stratospheric circulation and shorter soot lifetime than Mills et al. (2014), which has an interactive ocean and a horizontal resolution of  $1.9^\circ$  latitude by  $2.5^\circ$  longitude (Mills et al., 2014). Including NO emissions (IP vs. IP-NO) does slightly increase  $O_3$  loss, mostly by

slowing the recovery, but the effects are minor because the amount of NO injected is small and the temperature effects are so strong. Including aerosols in the photolysis calculations (IP vs. IP-AOD) slightly decreases the amount of  $O_3$  loss, but the effect is not significant.

Mills et al. (2008, 2014) did not include  $NO_x$  emissions and found that  $O_3$  loss was primarily driven by heating of the stratosphere and temperature dependencies in ozone decomposition and  $NO_x$  catalytic losses along with additional  $N_2O$  transport and longer  $NO_x$  lifetimes. Figure 3 shows the global average total column odd-oxygen chemical reaction rates for the IP (Figure 3b), IP-AOD (Figure 3a), and IP-NO (Figure 3c) cases as solid lines. The individual chemical reactions that are important to odd-oxygen chemistry and their contribution to these subtotals (Brasseur & Solomon, 2005) are shown in Table 2. Mills et al. (2008) did not output all of these individual rates, but their results should be similar to the IP-AOD case. Both cases show an increase in O production, which is primarily because of a temperature sensitivity in the photolysis cross section for the  $O_2 + h\nu \rightarrow 2O$  reaction. The IP case has lower overall reaction rates, because photolysis is reduced compared to the IP-AOD case by the reduced actinic flux caused by solar absorption from the soot. However, the total production and loss rates are greater than the control, indicating that the temperature effects are greater than the effects caused by the reduced actinic flux. There is a small increase in  $NO_x$  loss in the IP case compared to the IP-NO case, but the effects of the NO injection are negligible.

Looking at these rates relative to the total production of odd-oxygen (Figure 4) shows that  $HO_x$ ,  $ClO_x$ , and  $BrO_x$  catalytic cycles decrease relative to the control while the  $NO_x$  catalytic cycle and  $O_3$  decomposition ( $O_x$ ) increase. The magnitude of these changes is less when the aerosols are included in the photolysis calculation. Though  $HO_x$  remains the dominant odd-oxygen loss mechanism, as reported by Mills et al. (2008), increases in  $NO_x$  and  $O_x$  are the drivers of increased  $O_3$  loss following a nuclear conflict. The absolute contribution from  $HO_x$  stays fairly constant leading to a decreased relative contribution as odd-oxygen production increases. We also see both an absolute and relative decrease in the  $ClO_x$  and  $BrO_x$  catalytic cycles that was not seen by Mills et al. (2008). The  $O_x$ ,  $ClO_x$ , and  $BrO_x$  changes last about 2 years while  $NO_x$  changes last about 6 years.  $HO_x$  changes switch from relative decrease for 6 years to a slight relative increase for another 4 years.

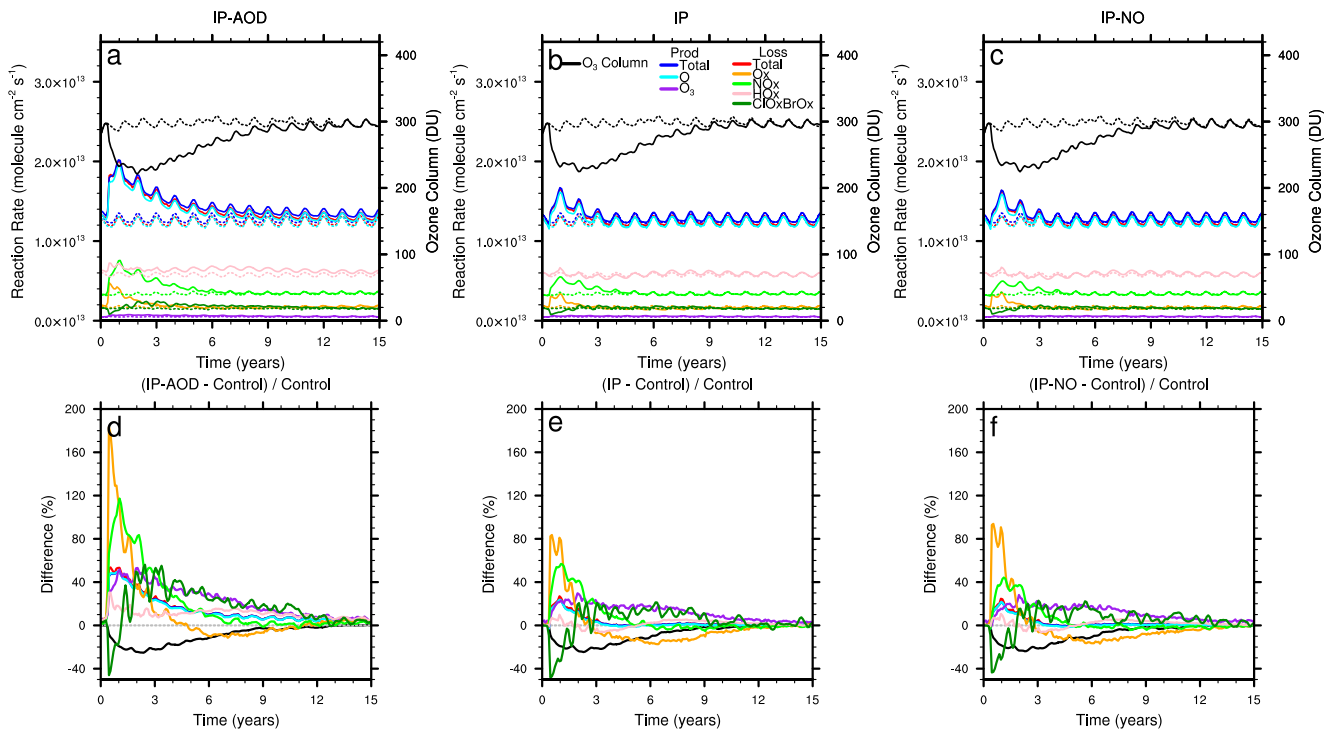


**Figure 3.** Evolution of column integrated absolute chemical reaction rates (color) and the  $O_3$  column (black) for the India-Pakistan (IP)-AOD (left), IP (center), and IP-NO (right) cases. The total reaction rates are on the top (a-c), and the percentage difference from the control case are on the bottom (d-f). The IP-AOD case does not include aerosols in the photolysis and the IP-NO case does not include any NO injection. The solid lines are the named case and the dotted lines are the control case. See Table 2 for the reactions included in each grouping.

Figure 5 shows the vertical profile of the global average chemical rates and  $O_3$  profile for the first year after the war for the IP-AOD and IP cases and the corresponding change in temperature is shown in Figure S4. The  $O_3$  profiles are similar for the IP-AOD and IP cases with reductions in the stratosphere and upper mesosphere. The IP-AOD case shows about a 20% increase in O production relative to the control in the stratosphere, but the IP case shows little change in O production relative to the control case when aerosols affect the actinic flux. Similarly, there is a large increase relative to the control in odd-oxygen loss from  $NO_x$  and  $O_x$  in the IP-AOD case in the stratosphere that is smaller in the IP case. In both cases,  $HO_x$  driven loss is increased in the stratosphere relative to the control, but reduced in the lower mesosphere and is nearly identical to the control in the troposphere and upper mesosphere contributing to the small change in  $HO_x$  loss rates seen in the total column (Figure 3).

Figure 6a shows the evolution of the change in zonal average column  $O_3$  for the IP case, while absolute amounts are shown in Figure S5b. Similar to Mills et al. (2014), we see a greater percentage loss, up to 60%, at higher latitudes and losses on the order of 10% in the equatorial tropics. As seen in the global average (Figure 2), the  $O_3$  recovers faster in our simulation than in Mills et al. (2014) because the soot particles get larger and have a shorter lifetime.

These  $O_3$  changes cause an increase in the surface UV Index (Figure 7b). The values shown are the monthly average of the daily maximum clear-sky values calculated by TUV. The daily maximum value should be close to the noon local time value that is commonly reported for UV Index; however, observed values at exactly noon local time or averaged over a 30 min period around noon local time may be lower than the maximum daily value by several points (Para et al., 2019). Compared to the control run (Figures 7a and S6a), there is an increased surface UV immediately following the war lasting for about 6 years. Since surface UV is a function of the Sun, aerosols, clouds, and  $O_3$ , the areas of the largest  $O_3$  depletion do not necessarily show the largest increases in surface UV. Values of 20 or larger are found between 30°S to 20°N the control case, but extend to 40°S to 40°N in the IP case. The largest increases in the IP case occur in the southern

**Table 2**

List of the Main Chemical Reactions Used in Whole Atmosphere Community Climate Model (WACCM) That are Important to Odd-Oxygen ( $O$  and  $O_3$ ) Concentrations

Type	Name	Weight	Reactions	
Production	O	2	$O_2 + h\nu \rightarrow O + O(^1D)$	
		2	$O_2 + h\nu \rightarrow 2 O$	
	$O_3$	1	$NO + HO_2 \rightarrow NO_2 + OH$	
		1	$CH_3O_2 + NO \rightarrow CH_2O + NO_2 + HO_2$	
Loss	$O_x$	2	$O + O_3 \rightarrow 2 O_2$	
		1	$O(^1D) + H_2O \rightarrow 2 OH$	
	$NO_x$	2	$NO_2 + O \rightarrow NO + O_2$	
		2	$NO_3 + h\nu \rightarrow NO + O_2$	
	$HO_x$	1	$HO_2 + O \rightarrow OH + O_2$	
		1	$HO_2 + O_3 \rightarrow OH + 2 O_2$	
		1	$OH + O \rightarrow H + O_2$	
	$ClO_xBrO_x$	1	1	$OH + O_3 \rightarrow HO_2 + O_2$
			1	$H + O_3 \rightarrow OH + O_2$
		2	2	$ClO + O \rightarrow Cl + O_2$
			2	$Cl_2O_2 + h\nu \rightarrow 2 Cl$
		2	2	$ClO + ClO \rightarrow 2 Cl + O_2$
			2	$ClO + ClO \rightarrow Cl_2 + O_2$
		2	2	$BrO + ClO \rightarrow Br + Cl + O_2$
			2	$BrO + ClO \rightarrow BrCl + O_2$
		2	2	$BrO + BrO \rightarrow 2 Br + O_2$
2			$BrO + O \rightarrow Br + O_2$	
1	$ClO + HO_2 \rightarrow O_2 + HOCl$			
1	$BrO + HO_2 \rightarrow HOBr + O_2$			

Note. These reactions are grouped by production and loss and by catalytic cycles for analysis purposes. The weight indicates the net odd-oxygen production or loss from a reaction. These weights are used to sum the individual reaction rates to calculate total production and loss rates.

polar region around 70°S, which is far removed from where the smoke was injected. The consequences of these changes in surface UV on the biota will be discussed in Section 3.3.

### 3.2. Global Nuclear War

Coupe et al. (2019) used WACCM4 to simulate the effects of a nuclear war between the United States and Russia using a scenario similar to Robock, Oman, and Stenchikov (2007), but with the same soot representation used in Toon et al. (2019). This study repeats Coupe et al. (2019) but includes in-line photolysis from TUV and  $NO_x$  emissions from the fireballs and the fires. Figure 8 shows the evolution of the change in column  $O_3$  for the NH (Figure 8a) and globally (Figure 8b). Connell & Wuebbles (shown in Pittock et al., 1986) used a photochemical model to assess  $O_3$  changes from three different weapons inventories from AMBIO (1982), Knox (1983), and NRC (1985) but only included effects from the fireball  $NO_x$  with no heating caused by the soot. The largest reduction they found was about 45% using the Knox (1983) inventory and the losses lasted about 10 years. Kao et al. (1990) included the effects of the soot and the fireball  $NO_x$ , but only in a short simulation that lasted 20 days. They used the NRC (1985) inventory, but achieved much larger loss of 15% in 20 days than Connell & Wuebbles did with the same inventory.

Coupe et al. (2019) showed that the stratospheric heating in the global war case is stronger than for a regional war and we show this heating results in  $O_3$  losses of up to 80% in the NH with losses lasting for 15 years. The difference in  $O_3$  loss between our extreme cases for  $NO_x$  emissions (UR-NO and UR + NO3) is up to 15% in the NH and 10% globally. Removing the aerosols from the actinic flux calculation (UR-AOD) results in less  $O_3$  loss by over 20% in the NH and 15% globally. The cause for this lower loss of  $O_3$  can be seen in the global average chemical reaction rates (Figure 9). The heating alone causes an almost three times increase in reaction rates (Figure 9a); however, when the aerosols are included in the actinic flux (Figure 9b), the reaction rates drop to less than a quarter of the unperturbed rates and more than compensate for the heating induced increase. Thus unlike the IP case, the reduction in actinic flux has a bigger impact on  $O_3$  than the temperature changes in the UR case as the total production and loss are much lower than seen in the control. Excluding the NO injection (Figure 9c) causes a small decrease in the  $NO_x$  loss for the first few years. The UR-AOD (Figure 10a) and UR (Figure 10b) cases show very different relative reaction rates. UR-AOD suggests that the

$HO_x$  cycle decreases initially and that the  $NO_x$  cycle and  $O_x$  decomposition drive the  $O_3$  loss, similar to what was seen in the IP case. However, in the UR case, the  $HO_x$  cycle actually increases for 15 years, while the  $NO_x$  cycle increases for 6 years and then decreases for 9.  $O_x$  decomposition decreases slightly and  $ClO_x$  and  $BrO_x$  cycles decrease for 10 years.  $O_3$  production in the troposphere takes on a more important role as  $O$  production is greatly diminished.

The global average vertical profile for the first year also shows significant differences between the UR-AOD (Figure 11a) and UR (Figure 11b) cases. In the UR case, all reaction rates in the stratosphere are significantly reduced compared to UR-AOD. Both simulations show a greatly reduced stratospheric  $O_3$  layer, with UR having a larger peak in the mesosphere than UR-AOD, where  $O$  production by photolysis is largely unaffected.

Figure 6b shows the evolution of the zonal average change in the  $O_3$  column for the UR case, while absolute amounts are in Figure S5c. Losses at mid to high latitude exceed 75% and over 65% in the tropics during the first few years. Recovery in the tropics is faster than at high latitude, but still takes 10 years to recover to

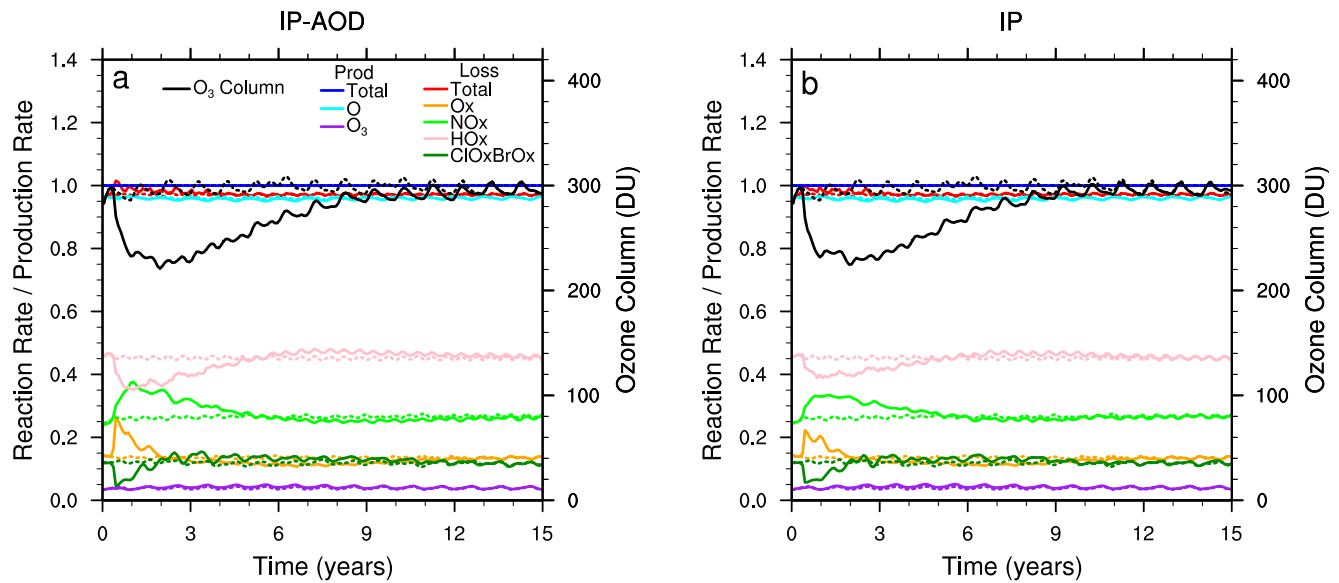


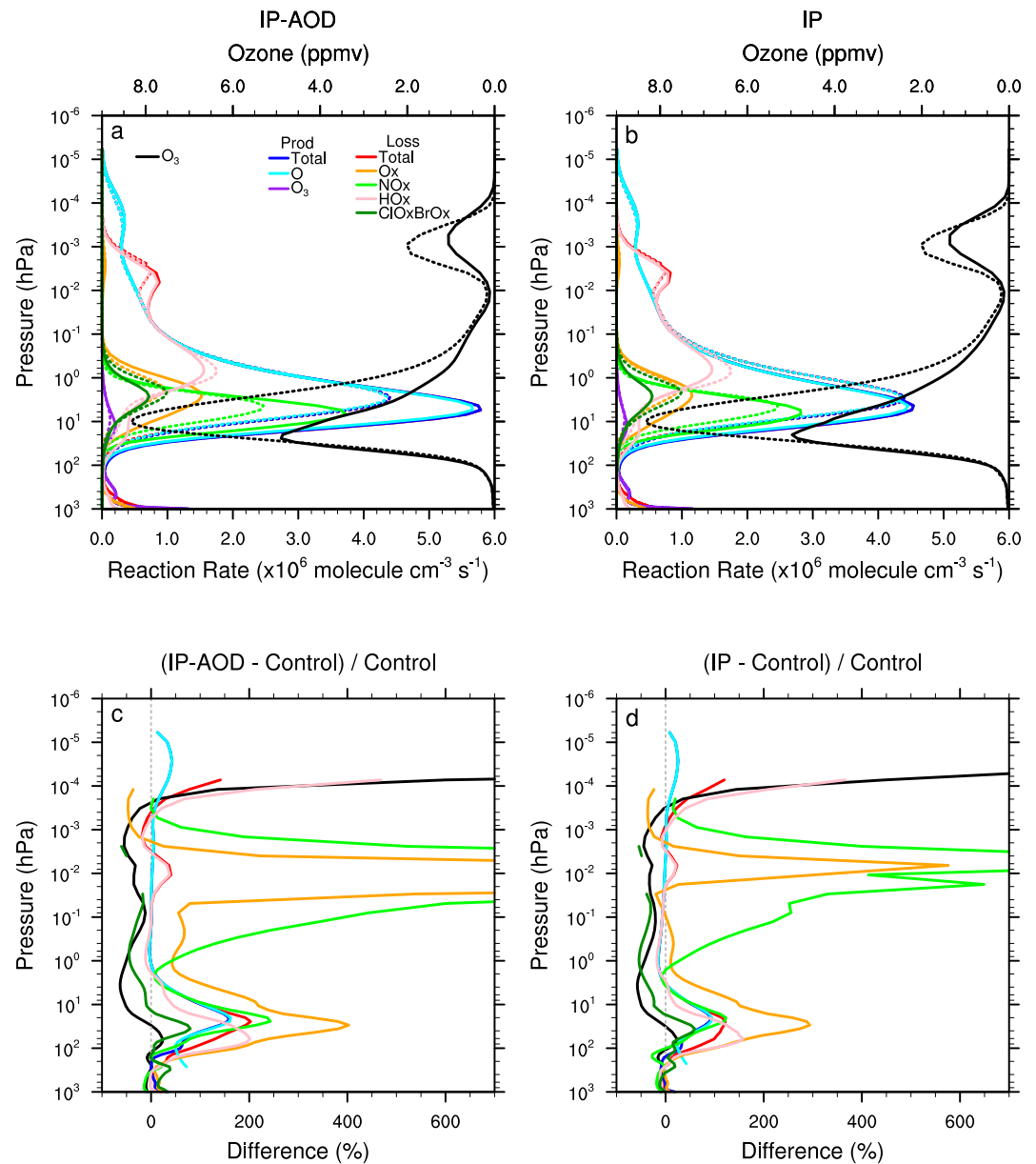
**Figure 4.** Similar to Figure 2, but for column integrated chemical reaction rates relative to the evolving total production rate of the respective case. Thus, by definition the total production for each of these cases, both the perturbation and the control, is 1.0.

within 5% of the control case. Initially, the soot compensates for the  $O_3$  loss and UV is actually reduced at the surface (Figures 7c and S6b) compared to the control (Figure 7a). However, the UV Index begins to increase relative to the control after 3 years as the soot clears reaching a peak 8–9 years after the war. UV Index values of 35 are seen in the tropics from years 5–8, and are greater than 45 during the summer in the southern polar regions from years 5 to 8. Maps of UV Index for selected months averaged over years 8 to 10 show a generally zonal structure but with regions of extreme UV including higher altitudes and deserts (Figure S8).

### 3.3. Effects of Surface UV Changes

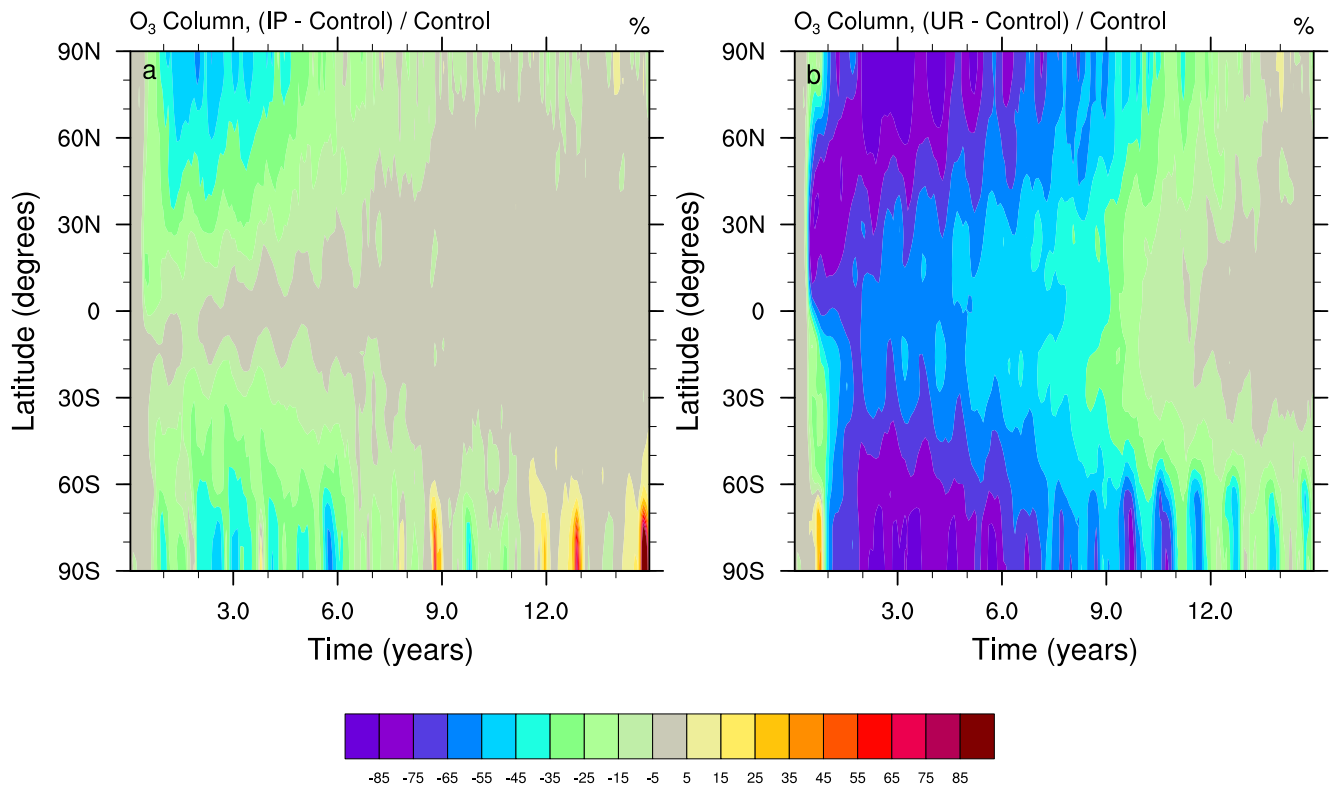
Soot injected into the atmosphere absorbs sunlight heating the stratosphere and reducing the solar radiation at the surface causing lower surface temperatures and reduced precipitation. The heating in the stratosphere causes increased  $O_3$  destruction that allows more UV radiation to the surface. Effects from these climatic changes for regional wars have been discussed in Robock, Oman, Stenchikov, Toon et al. (2007), Stenke et al. (2013), Mills et al. (2014), and Toon et al. (2019). Jägermeyr et al. (2020) found large agricultural changes and Scherrer et al. (2020) predicted significant effects on fisheries in response to climatic changes from a regional nuclear war. Scherrer et al. (2020) also found larger effects for the global war case. However, neither study included the effects of  $O_3$  or UV changes, which would likely lead to additional losses especially related to global grain productivity. The effects of a global nuclear war were studied in the 1980s (e.g., Crutzen & Birks., 1982; Harwell & Hutchinson., 1986; Turco et al., 1983), but these studies did not include the effects of stratospheric heating on  $O_3$  loss. Robock, Oman, and Stenchikov (2007) and Coupe et al. (2019) revisited these global war studies, but did not include estimates of changes to stratospheric  $O_3$  or surface UV.

Figure 12 shows the evolution of global average aerosol optical depth (AOD), surface temperature, precipitation,  $O_3$ , PAR, UV-A, and UV-B for the IP and UR cases. In both cases, PAR and UV-A is reduced by the presence of the aerosol, but UV-B responds differently in the two cases. The major absorber for UV-B is  $O_3$ , so in the IP case (Figure 12a), which added a smaller amount of soot but still has significantly lowered  $O_3$ , UV-B increases by up to 10% in proportion to the  $O_3$  destruction. For the UR case (Figure 12b), so much soot is injected that even though the  $O_3$  loss is greater than in the IP case, there is still a dramatic reduction in UV-B, UV-A, and PAR. However, in the UR case, the soot is removed faster than the  $O_3$  recovery, so after 7 years there is a net 20% increase in UV-B. UV-B remains elevated for eight more years, while PAR recovers after 10 years. Photosynthetic organisms in terrestrial and marine environments are sensitive to the ratios of UV-B, UV-A, and PAR (Krizek, 2004). High levels of UV-B can contribute to inhibition of photolysis



**Figure 5.** Global average vertical profile of absolute reaction rates (colors) and  $O_3$  (black) for the first year following the war for the India-Pakistan (IP)-AOD and IP cases. In both cases, the solid lines are the named case and the dotted lines are the control. Note the  $O_3$  scale is increasing to the left.

affecting photosystem II (Hakala-Yatkin et al., 2010; Kataria et al., 2014; Ragni et al., 2008) reducing leaf expansion (e.g., Searles et al., 2001) and plant growth rate (Allen et al., 1998; Ballaré et al., 2001, 2011). However, some UV-B damage may be offset by supplemental PAR and UV-A radiation involved in the repair process (Krizek, 2004) with plants adapting to higher UV-B by producing compounds such as plant pigmentation which might improve the quality of certain crops (Bassman, 2004; Bornman et al., 2015). Unfortunately, in our nuclear war scenarios we see increased UV-B along with decreased UV-A and PAR, suggesting photosystem II damage and a simultaneous slowing of repair processes. In the IP case, PAR, UV-A, and UV-B return to within a few percent of normal levels at the same time; however, in the UR case UV-A and PAR return to within a few percent of normal levels 5 years before UV-B which may offset some of the potential damage.



**Figure 6.** Evolution of the zonal average percent change in the O<sub>3</sub> column from the control for the India-Pakistan (left) and UR (right) cases.

UV can have both beneficial and harmful effects on humans. UV-B is needed for vitamin D synthesis and UV-A helps prevent seasonal affective disorder, a type of depression associated with the change of seasons (MacKie, 2000). Vitamin D deficiency can lead to rickets, a disease that can cause weak or soft bones in children and a similar disease called osteomalacia in the elderly. Because of this, vitamin D is often added as a food supplement, for example, to milk. Vitamin D deficiency has also been linked to chronic diseases like cardiovascular disease and cancer, and it is especially prevalent in minority groups, likely due to a

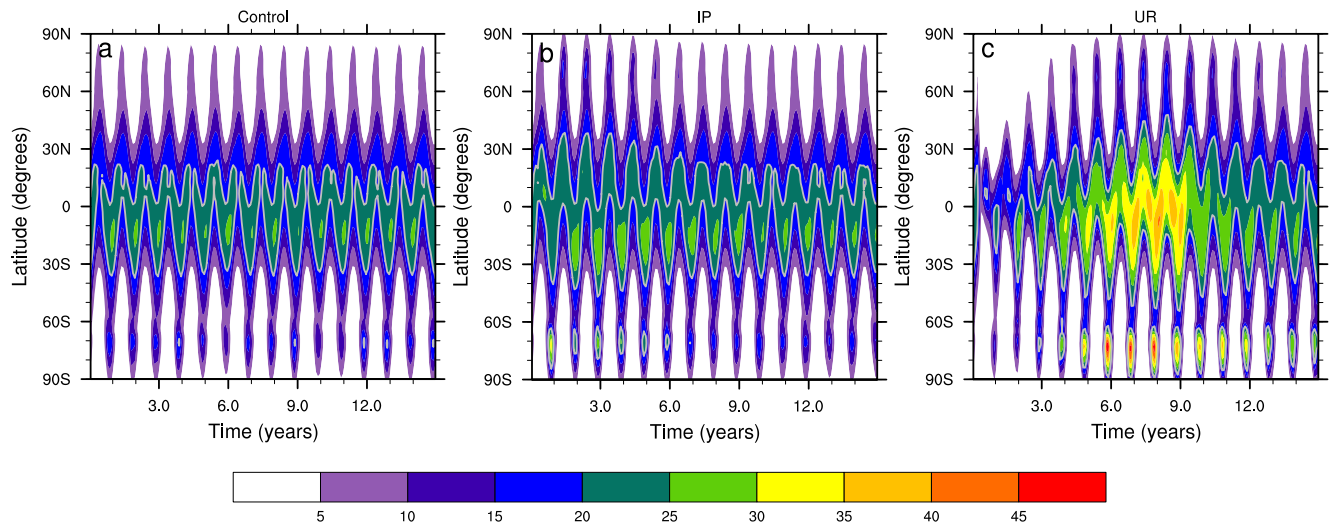


**Figure 7.** Evolution of zonal and monthly averages of the daily maximum clear-sky surface ultraviolet (UV) Index for the control (left), India-Pakistan (IP) (middle), and UR (right) cases. The maximum values are 26, 33, and 50 respectively. The gray line shows the UV Index of the 20 contour to highlight the expansion of areas of extreme UV in the IP and UR cases.

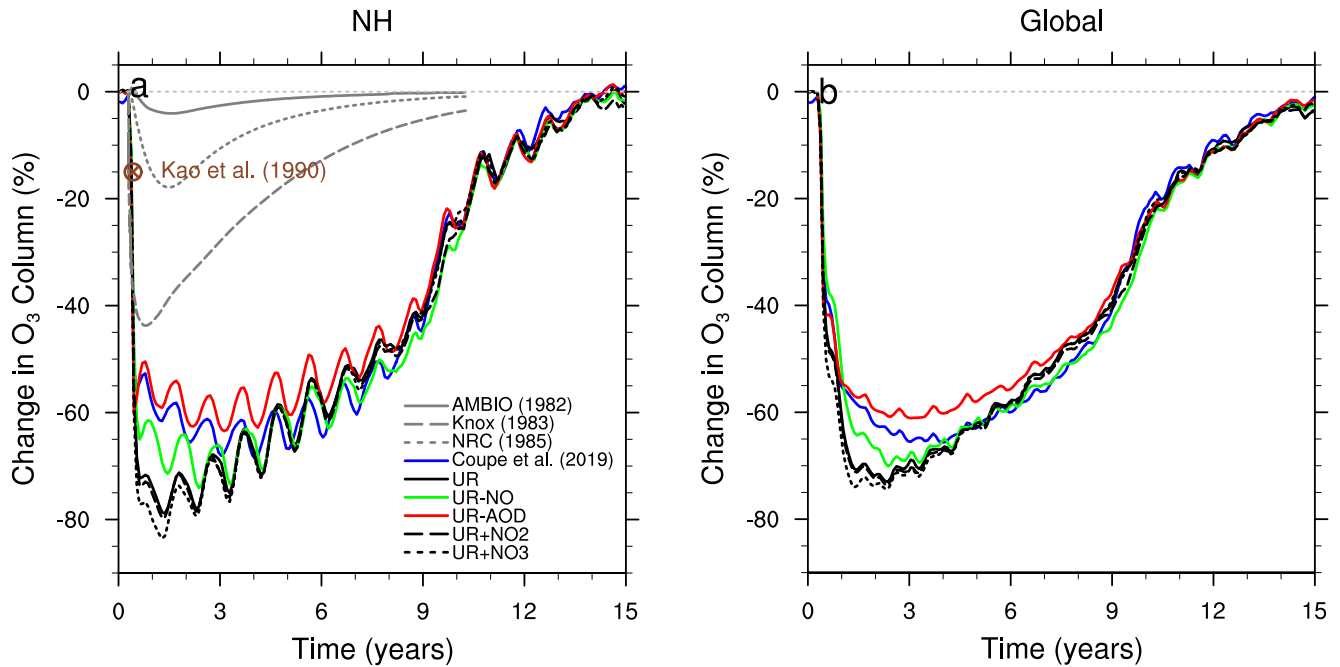


**Figure 8.** Evolution of the change in global average column  $O_3$  in the Northern Hemisphere from Pittcock et al. (1986) using scenarios from AMBIO (1982), Knox (1983), and NRC (1985) along with Whole Atmosphere Community Climate Model version 4 (WACCM4) simulations from Coupe et al. (2019), UR, UR-NO, UR-AOD, UR + NO<sub>2</sub>, and UR + NO<sub>3</sub> (left) and global averages (right) for just the WACCM4 simulations. Kao et al. (1990) only provided information about the end of their 20-day simulation. See Table 1 for the abbreviations and descriptions of the United States/Russia (UR) cases from this study.

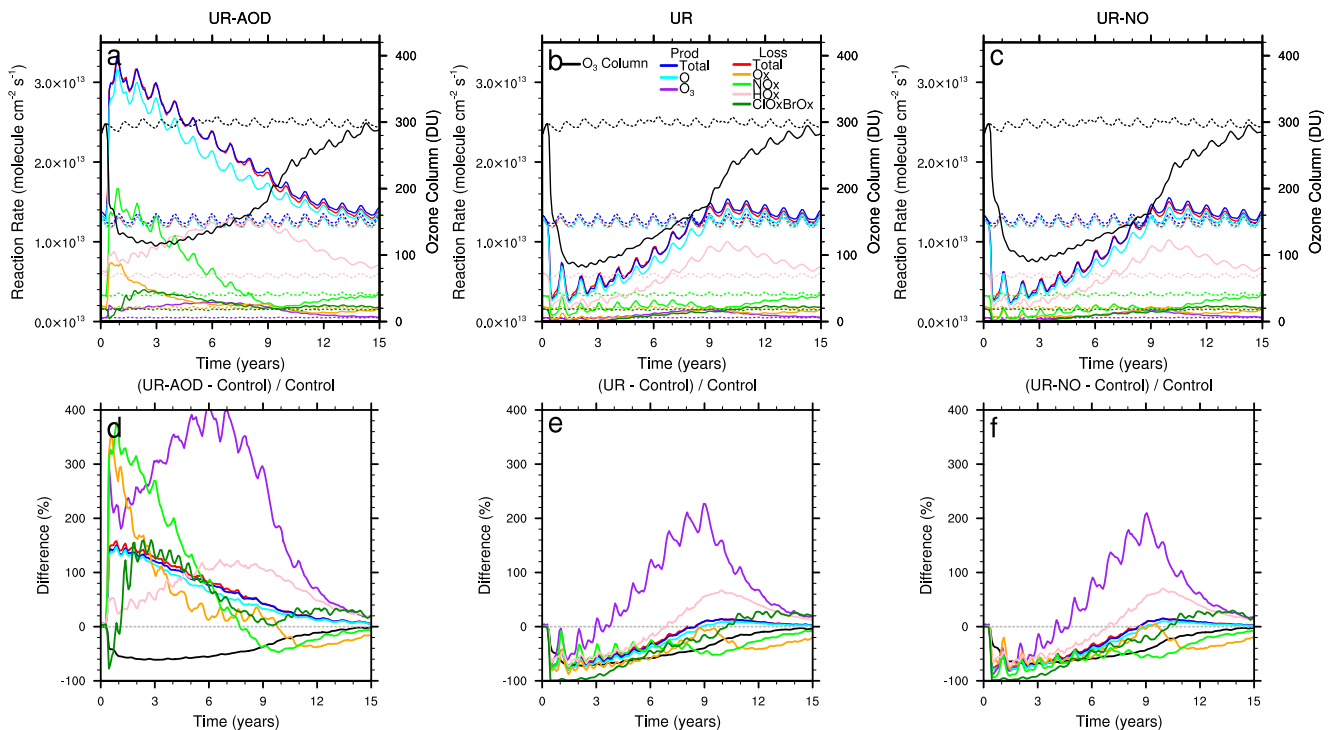


**Figure 9.** Similar to Figure 3, but for the UR-AOD (left), UR (center), and UR-NO (right) cases.

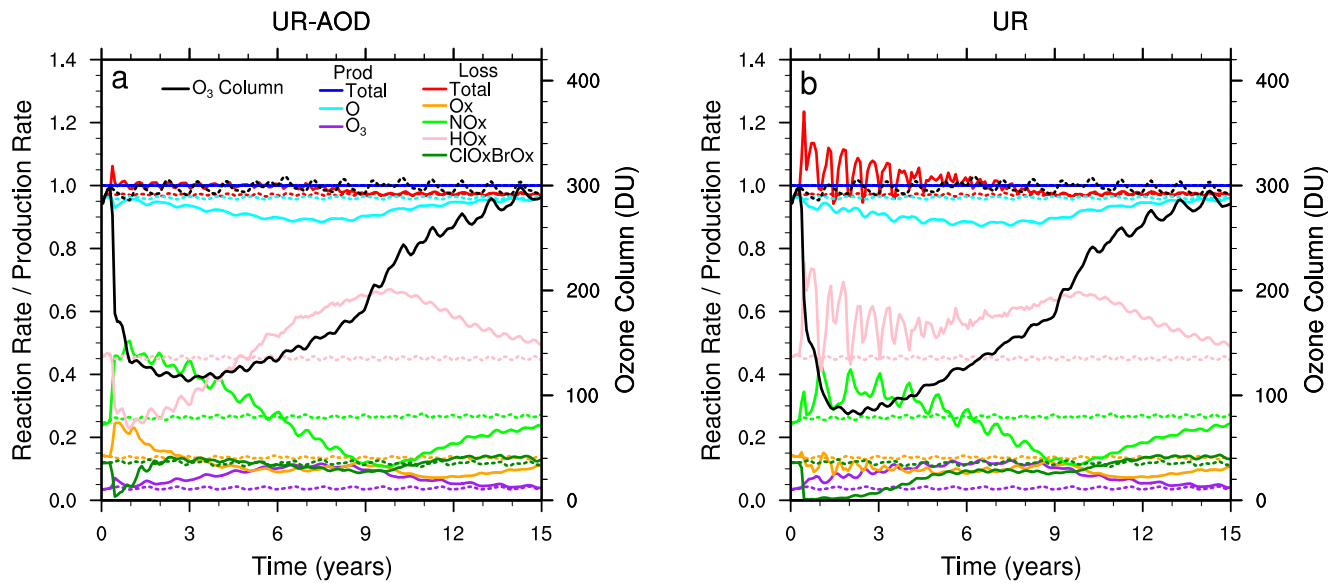
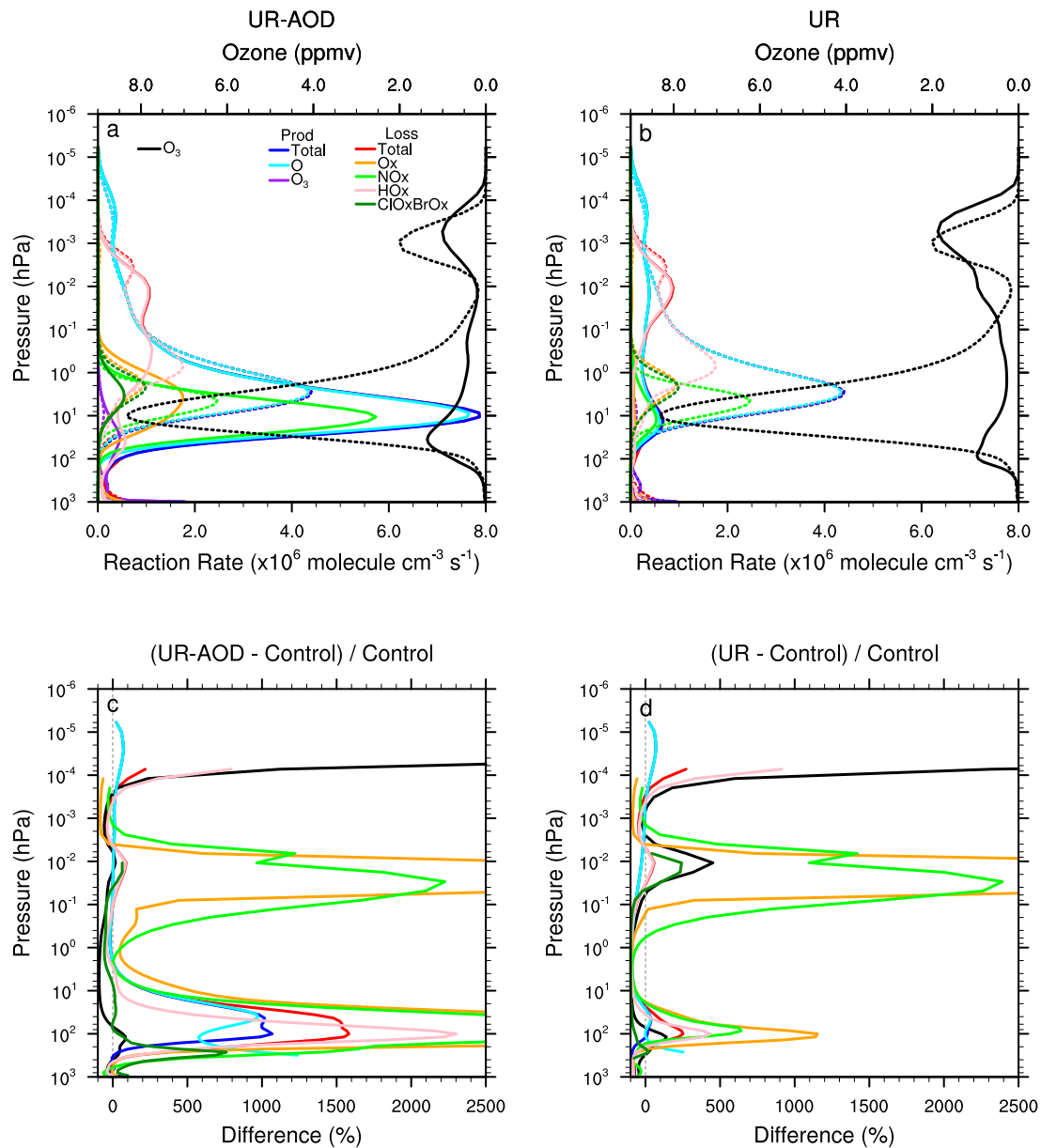


Figure 10. Similar to Figure 4, but for the UR–AOD (left) and UR (right) cases.

combination of genetic (pigmentation) and socioeconomic factors (Forrest & Stuhldreher, 2011). On the other hand, there are several serious harmful effects of increased UV-B including sunburn, photoaging, skin cancer, and cataracts (MacKie, 2000). People with either a genetic or drug-induced sensitivity to UV or who are genetically unable to repair DNA damage may be particularly affected. UV-C (200–280 nm) is readily absorbed by O<sub>3</sub> and thus does not reach the surface and is generally not considered in terms of effects on human health (MacKie, 2000).

To better understand the role of UV radiation on biota, various action spectra have been identified that integrate a portion of the spectrum that is important for particular biological processes. Figure 13 shows examples of changes in the action spectra calculated by TUV for plant growth (Flint & Caldwell., 2003), phytoplankton inhibition (Boucher et al., 1994), vitamin-D synthesis (Bouillon et al., 2006), cataract formation (Oriowo et al., 2001), solar induced erythema (Anders et al., 1995), and DNA damage (Setlow, 1974) along with the UV-B spectrum for the IP and UR cases. The changes in the action spectra generally follow the shape of UV-B, but the magnitudes may be different. For the IP case (Figure 13a) these are generally positive for 10 years following the war. Plant growth, which refers to the height of light-grown oat seedlings, is the only one that experiences a negative change which persists for 2 years. The largest increase of up to 40% is for DNA damage, a proxy for forming human skin cancers. The next largest is erythema (sunburn) which increases at up to 28% closely followed by vitamin-D synthesis. Cataract damage, the formation of cloudy spots on pig eye lenses, closely matches the changes in UV-B, with up to a 19% increase. Finally, UV inhibition of phytoplankton carbon absorption, increases by up to 11%. The UR case (Figure 13b) shows the same general relationship between the magnitudes of the different action spectra. However, each action spectra first experiences negative changes with a 90% reduction and then becomes positive after a period of time. Vitamin-D synthesis is negative for the first 4 years, indicating a brief period of extreme risk for rickets. The DNA damage metric becomes positive within a year and reaches a peak increase of 140%. The others show positive values after 4–7 years, with peak increases between 10% and 60%.

UV that could cause DNA damage increases rapidly in the UR case because of the shapes of the O<sub>3</sub> and soot absorption spectra. Figure 14a shows the O<sub>3</sub> absorption cross-section (Gorshlev et al., 2014) and the soot mass absorption coefficient for 0.16 μm particles in the range of 230–370 nm, both normalized by the maximum value within that range. O<sub>3</sub> has a very strong peak around 255 nm, but does absorb across this entire wavelength range. Soot absorption decreases by 40% from 230 to 370 nm. Figure 14 shows the evolution of changes in UV-B and action spectra related to human skin cancer: erythema, DNA damage, and skin cancer (de Gruuji & Van der Leun, 1994; CIE, 2006) for the IP and UR cases. In the control (not shown) O<sub>3</sub> absorbs essentially all of the UV-C and a large fraction of the UV-B light. In the IP case (Figure 14b), the moderate



**Figure 11.** Similar to Figure 5, but for the UR–AOD (left) and UR (right) cases. Note the O<sub>3</sub> scale is increasing toward the left in panels (a) and (b).

loss of O<sub>3</sub> causes an increase in surface UV. In the UR case (Figure 14c), even though there is a much larger loss of O<sub>3</sub>, there is a decrease in surface UV-B because of the large UV absorption by the soot. As the soot is removed, the surface UV increases gradually over 8 years. UV-B is larger compared to the control starting 4–7 years after the war, depending on the exact spectral weights of the action function. However, lost O<sub>3</sub> absorption in the UV-C range, that could cause DNA damage and where O<sub>3</sub> is most absorbing, is not compensated for by the increased but relatively weaker soot absorption. This leads to the rapid and large increase of DNA damaging UV in the UR case; however, this increase is from very low levels, so UV-C is still probably not a health threat for either nuclear war case. UV-C changes may need to be accounted for when O<sub>3</sub> loss is larger, for example following fires generated by an asteroid impact at the K-Pg boundary (Bardeen et al., 2017).

While CESM is capable of simulating the ocean physical, biogeochemical, and ecological response to nuclear war (e.g., Coupe et al., 2021; Lovenduski et al., 2020; Scherrer et al., 2020), the version of CESM used in this study does not include the effect of UV inhibition on phytoplankton growth, which may affect

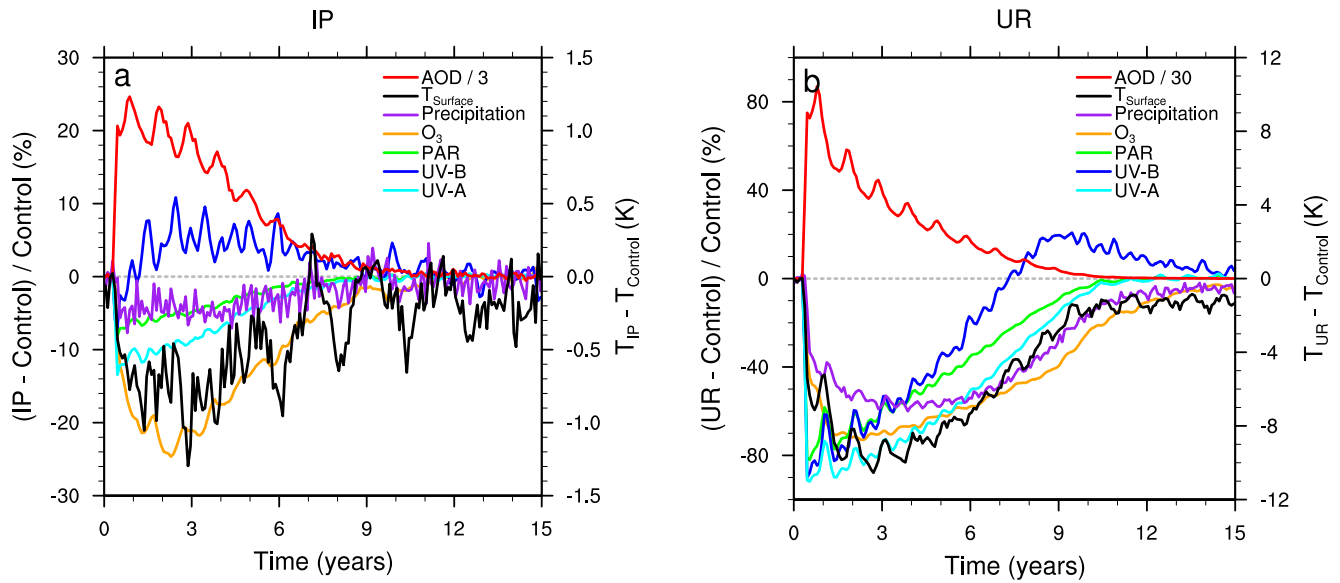


**Figure 12.** Evolution of the change in the global average for surface values of aerosol optical depth, temperature, O<sub>3</sub> column, and precipitation compared with the spectral integrals of photosynthetically available radiation and ultraviolet-B for the India-Pakistan (IP) (left) and UR (right) cases. Temperature (black) is on the right scale and the percentage change of the other fields (color) are on the left scale. AOD is the total aerosol optical depth including both the soot and the background aerosol and has been reduced by a factor of three in the IP case and 30 in the UR case to fit on the plot. The maximum global average AOD values are 0.13 for the control, 0.20 for the IP case, and 2.92 for the UR case.

each taxa differently (De Tommasi et al., 2018; Jeffrey et al., 1999; Xu et al., 2016). Diatoms, which are the dominant phytoplankton functional type outside the oligotrophic subtropical gyres, have a silica shell that may provide UV protection, while in the gyres small phytoplankton dominate, which with the exception of coccolithophores have no known UV protection. Future work will address this issue by including

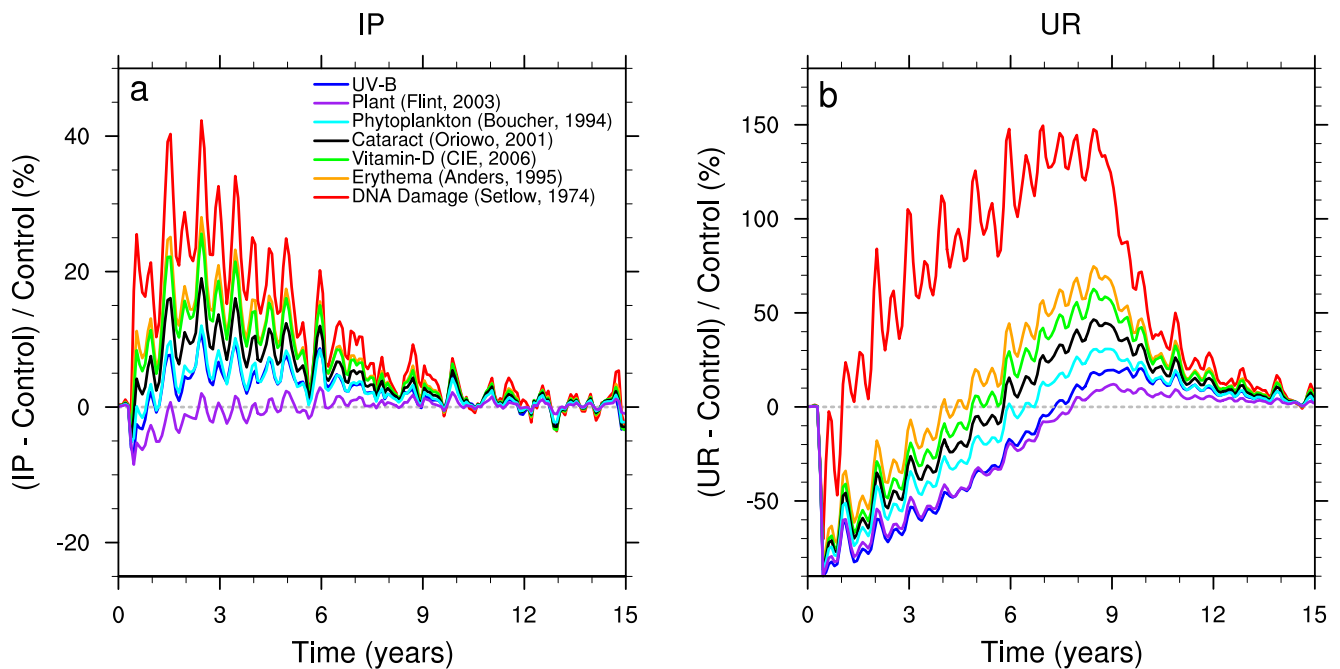


**Figure 13.** Evolution of the change in the global average surface values for ultraviolet-B compared with the action functions for plant growth, inhibition of phytoplankton, cataract formation, vitamin-D synthesis, erythema, and DNA damage for the India-Pakistan (IP) (left) and UR (right) cases. Note the different vertical scales for the two panels.

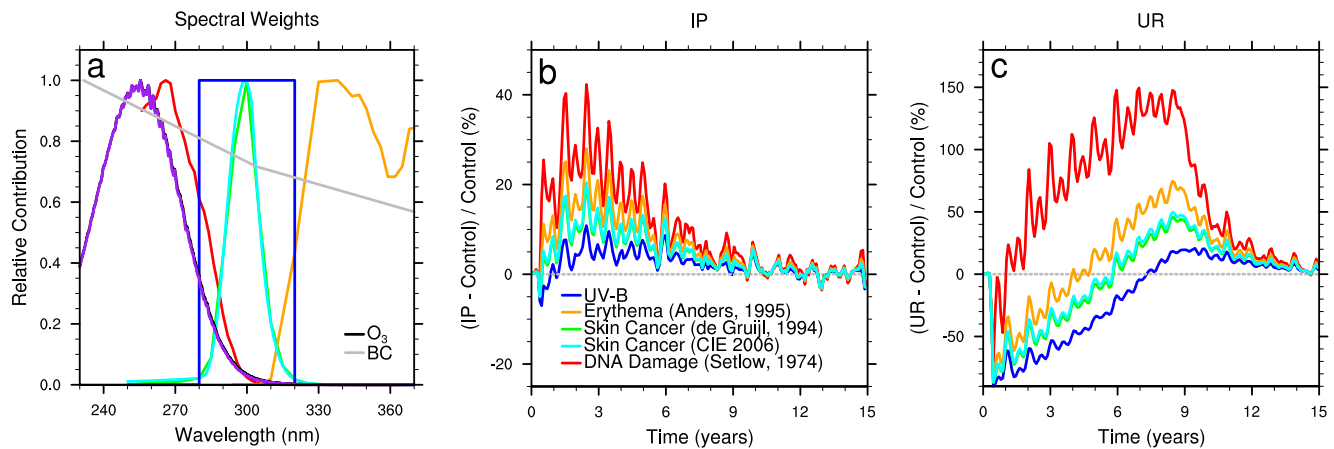


**Figure 14.** ultraviolet (UV) spectra for O<sub>3</sub> absorption cross-section (black) and soot mass absorption coefficient (gray) along with spectral weighting functions for UV-B, erythema, DNA damage, and two metrics for non-melanoma skin cancer over the range 230–370 nm (left). Evolution of the change in the global average spectral integrals of UV-B compared with the action functions for erythema, DNA damage and non-melanoma skin cancer for the India-Pakistan (IP) (center) and UR (right) cases. Note the different vertical scales for these two panels.

a representation of UV inhibition in lower trophic levels. Changes in phytoplankton will in turn influence their consumers, that is, fish and other higher trophic-level organisms (Stock et al., 2017). In this way, the war-driven changes in UV might have bottom-up effects on fish and fisheries that could be estimated in future work. Experiments indicate that many shallow-living marine organisms and freshwater fish are directly harmed by increasing levels of UV-A and UV-B (Alves & Agustí, 2020; Llabrés et al., 2013). However, the direct effects of UV on the fish in the wild are poorly known, leaving the impact of UV changes on fish and fisheries highly uncertain.

UV effects on plant growth are complex and currently not represented in most crop and land surface models (Wargent & Jordan, 2013), but recent model development is trying to address and quantify related processes. Surface O<sub>3</sub> also changes in these simulations (Figure S7) and can have severe impacts on plant growth and crop yields by decreasing plant photosynthesis rates and stomatal conductance (Lombardo et al., 2012, 2013). Surface O<sub>3</sub> is strongly affected by the Stratosphere-Troposphere-Exchange (STE) and tropospheric photochemistry (Xia et al., 2017). While these simulations do show a significant change in surface O<sub>3</sub> from STE, they do not include detailed tropospheric chemistry and thus cannot fully assess the changes to surface O<sub>3</sub>. Impacts of surface O<sub>3</sub> on plants and crop yields are not currently simulated by Earth System models or most process-based crop models (Schauberger et al., 2019); however, there are an increasing number of pilot studies including an O<sub>3</sub> damage function in land models (Lombardo et al., 2015) and crop models (Emberson et al., 2018).

CESM does not have a built-in capability to track effects upon human health, but the availability of these action spectra could enable additional capabilities in the future. Humans if properly informed and equipped have the ability to adapt to these changes by staying indoors, only going out at night, or by covering up with clothes and sunscreens. Plants and animals are also sensitive to these changes. While ranchers may be able to make adaptations for livestock, wild populations of plants and animals will be exposed to the direct effects of these UV changes.

#### 4. Conclusions

In this study, we conducted simulations of regional and global scale nuclear war impacts on ozone using a modified version of WACCM4 that for the first time includes in-line calculations of actinic flux using TUV. This allows for the inclusion of aerosols in the photolysis calculation and for the diagnostic output of action spectra that can help quantify ecosystem and health effects. We also included the emissions of NO from the fireball and the surface fires. For regional wars, we find that while including aerosols in the photolysis calculation does change reaction rates, the effects of this and NO emissions does not make a significant change in the O<sub>3</sub> loss relative to earlier calculations that did not include them. This results in a peak global

average loss of ~25% with much larger losses of up to 55% at high latitudes. We find that the HO<sub>x</sub> catalytic cycle remains the largest loss mechanism, but is largely unchanged as found by Mills et al. (2008). Also, as reported by Mills et al. (2008), the increase in the NO<sub>x</sub> cycle and O<sub>x</sub> decomposition drive the increased O<sub>3</sub> loss. We see a reduction in loss from the ClO<sub>x</sub> and BrO<sub>x</sub> cycles that was not reported previously.

For global nuclear war, we provide the first estimates of O<sub>3</sub> and surface UV from modern climate models and find much greater O<sub>3</sub> loss than was predicted in the 1980s, with a peak global average loss of 75%. While the weapon sizes and therefore NO emissions have decreased since the 1980s, the inclusion of smoke and the heating of the stratosphere causes significant O<sub>3</sub> loss as demonstrated by Kao et al. (1990) and shown for regional wars by Mills et al. (2008). For the global war, the inclusion of aerosols in the photolysis calculations show large changes in chemical reaction rates and 15% larger peak O<sub>3</sub> loss. We also show that reduced O production and the HO<sub>x</sub> cycle dominate the increased O<sub>3</sub> loss with a contribution from the NO<sub>x</sub> cycle for the first few years.

The warming of the higher polar latitudes (Figures S2, S3 and S4) in both the IP and UR cases greatly reduces the importance of the standard chlorine and bromine heterogeneous chemistry for O<sub>3</sub> depletion. For the UR case, the zonal winds are significantly altered compared to the control and the overall stratospheric Brewer Dobson circulation changes affect the transport of odd-oxygen loss precursors into the polar lower stratosphere. Poleward and downward transport of NO<sub>x</sub> is increased by more than 150% in the IP case and more than 400% in the UR case relative to the control. Increased stratospheric H<sub>2</sub>O from a warmer tropopause increases H<sub>2</sub>O in the SH polar region to values greater than 8 ppmv and 150 ppmv relative to the control in the IP and UR cases respectively. Consequently HO<sub>x</sub> is also increased by over 100% and 500% in these two cases (Figure S2). Air depleted of O<sub>3</sub> is also transported from the upper/middle stratosphere into the lower polar stratosphere. Depletion of total column ozone (TCO) is much greater for the six years after the IP event than in the control (Figure 6 and S5). This depletion is not limited to just the September and October periods, but throughout the SH polar season due to increases in NO<sub>x</sub> and HO<sub>x</sub>. The IP event would cause a short-term hiatus in the recovery of TCO (e.g., Solomon et al., 2016) of approximately 10 years. TCO depletion from the UR case in the SH polar latitudes is extreme, with a minimum TCO of less than 75 DU extending from the pole to 50°S for the first 6 years following the war. This depletion is not only seen in the SH polar region, but also the NH polar region.

Surface UV is affected by both the O<sub>3</sub> loss, which increases surface UV, and the smoke injection, which decreases surface UV. For the regional war, the smoke injection is small enough relative to the O<sub>3</sub> destruction that there is an increase in surface UV for the entire period following the war that is proportional to the amount of the O<sub>3</sub> loss. For the global war, while the O<sub>3</sub> loss is extremely large, the smoke injection is so big that it leads to reduced UV at the surface for the first few years following the war. The rate of O<sub>3</sub> recovery lags the smoke removal and thus there are several years of very high surface UV, with a UV Index over 35 following a global nuclear war. Thus, following a regional war the climatic changes and the surface UV changes occur at the same time, shortening the period of large change and providing a uniform threat that decreases with time. However, for the global war the climatic changes come first followed by the elevated surface UV. This extends the period of changed conditions and causes the nature of the change to switch from reduced light, surface temperature and precipitation to one of increased surface UV. This means that adaptations that may have worked in first few years following the global war may not work as the surface UV increases. Changes in spectral integrals show that greatest increase is for DNA damage, which increases by up to 140% in the global war case and there is a risk of insufficient vitamin-D during the first few years following a global war. Assessments of impacts on agriculture and fisheries like those done by Jägermeyr et al. (2020) and Scherrer et al. (2020) for a regional nuclear war need to include the effects of UV and surface O<sub>3</sub> changes, and need to be done for the larger and differently sequenced effects that are generated by a global nuclear war.

A new version of the WACCM model has been released (Gettelman et al., 2019) with improved atmospheric physics including interactive modal aerosols, stratospheric aerosols, a new boundary layer and shallow convection scheme, a new cloud scheme that includes the aerosol indirect effect, and improved biogeochemistry in the land and the ocean models. Initial experiments with this model have shown it to be unstable when presented with the large perturbations considered here, so further work is needed before using it for nuclear war simulations. We also plan to explore the addition of organic and sulphate coatings on the

soot. Yu et al. (2019, 2020) have shown that wildfire smoke lofted into the stratosphere is coated with large amounts of organics. They speculated on whether the smoke might become coated in sulphate and contribute surface area to heterogeneous chemistry. Because of the different fuels, urban fires (as in a nuclear war scenario) would likely have less of an organic coating than wildfire smoke, but such a coating would provide a “lensing” effect that increases the particle absorption (Bond et al., 2006) and the larger particles would likely have a shorter lifetime in the stratosphere. This could affect both the intensity and the duration of climatic changes following a nuclear war.

The ability to calculate and output spectral action functions allows for a better assessment of the threats posed to the biota by a nuclear war. It also opens up the possibility for these data to be coupled with surface models allowing the effects of the detailed changes in surface light spectra to be included in parameterizations of the effects on the biota including those for phytoplankton and vegetation. There is a need for parameterizations of biological effects to be developed for the large UV increases that are predicted here and for climatic conditions that are cooling rather than for the warming conditions that have generally been evaluated for studies of the ozone hole and anthropogenic climate change. Action spectra also provide data that can be used for assessment of human health impacts. These model improvements would be beneficial for simulation of other types of climate change driven by large aerosol injections including volcanic eruptions, mass fires, dust storms, and solar geoengineering.

### Data Availability Statement

The CESM model is freely available from NCAR, but requires registration at [www.cesm.ucar.edu/models/cesm1.2](http://www.cesm.ucar.edu/models/cesm1.2). All the data and scripts needed for the plots presented in this paper and the supplement are publicly available from [osf.io/Bardeen\\_2021\\_OzoneUV](https://osf.io/Bardeen_2021_OzoneUV) (<https://doi.org/10.17605/OSF.IO/KVY86>). The full model output is very large and is stored on the PetaLibrary at the University of Colorado, which is not available to the public. However, additional data from these runs can be provided upon request.

### Acknowledgments

This work was funded by the Open Philanthropy Project. This work utilized resources from the University of Colorado Boulder Research Computing Group, which is supported by the National Science Foundation (awards ACI-1532235 and ACI-1532236), the University of Colorado Boulder, and Colorado State University. Thanks to Sasha Madronich for his help with TUV and to Richard Turco for his comments on the manuscript.

### References

- Aleksandrov, V. V., & Stenchikov, G. L. (1983). On the modeling of the climatic consequences of the nuclear war. *Proceedings in Applied Mathematics*, Comput. Cent. (p. 21): Russian Academy of Sciences.
- Allen, D. J., Nogués, S., & Baker, N. R. (1998). Ozone depletion and increased UV-B radiation: Is there a real threat to photosynthesis? *Journal of Experimental Botany*, *49*, 1775–1788. <https://doi.org/10.1093/jxb/49.328.1775>
- Alves, R. N., & Agusti, S. (2020). Effect of ultraviolet radiation (UVR) on the life stages of fish. *Reviews in Fish Biology and Fisheries*, *30*, 335–372. <https://doi.org/10.1007/s11160-020-09603-1>
- AMBIO, Barnaby, F., Kristoferson, L., Peterson, J., Prawitz, J., Rodhe, H., & Rotblat, J. (1982). Reference Scenario: How A Nuclear War Might Be Fought. *Ambio* (Vol. 11, pp. 94–99).
- Anders, A., Altheide, H.-J., Knälmann, M., & Tronnier, H. (1995). Action spectrum for erythema in humans investigated with dye lasers. *Photochemistry and Photobiology*, *61*, 200–205. <https://doi.org/10.1111/j.1751-1097.1995.tb03961.x>
- Andreae, M. O. (2019). Emission of trace gases and aerosols from biomass burning—An updated assessment. *Atmospheric Chemistry and Physics*, *19*, 8523–8546. <https://doi.org/10.5194/acp-19-8523-2019>
- Ballaré, C. L., Caldwell, S. D., Flint, S. D. S. A., & Bornman, J. F. (2011). Effects of solar ultraviolet radiation on terrestrial ecosystems: Patterns, mechanisms, and interactions with climate change. *Photochemical and Photobiological Sciences*, *10*, 226–241. <https://doi.org/10.1039/C0PP90035D>
- Ballaré, C. L., Rousseaux, M. C., Searles, P. S., Zahler, J. G., Giordano, C. V., Robson, M., et al. (2001). Impacts of solar ultraviolet-B radiation on terrestrial ecosystems of Tierra del Fuego (southern Argentina) An overview of recent progress. *Journal of Photochemistry and Photobiology B: Biology*, *62*, 67–77. [https://doi.org/10.1016/S1011-1344\(01\)00152-X](https://doi.org/10.1016/S1011-1344(01)00152-X)
- Bardeen, C. G., Garcia, R. R., Toon, O. B., & Conley, A. J. (2017). On transient climate change at the Cretaceous—Paleogene boundary due to atmospheric soot injections. *Proceedings of the National Academy of Sciences of the United States of America*, *114*, E7415–E7424. <https://doi.org/10.1073/pnas.1708980114>
- Bardeen, C. G., Toon, O. B., Jensen, E. J., Marsh, D. R., & Harvey, V. L. (2008). Numerical simulations of the three-dimensional distribution of meteoric dust in the mesosphere and upper stratosphere. *Journal of Geophysical Research*, *113*, D17202. <https://doi.org/10.1029/2007JD009515>
- Bassman, J. H. (2004). Ecosystem consequences of enhanced solar ultraviolet radiation: Secondary plant metabolites as mediators of multiple trophic interactions in terrestrial plant communities. *Photochemistry and Photobiology*, *79*, 382–398. <https://doi.org/10.1111/j.1751-1097.2004.tb00025.x>
- Bonan, G. B., Lawrence, P. J., Oleson, K. W., Levis, S., Jung, M., Reichstein, M., et al. (2011). Improving canopy processes in the Community Land Model version 4 (CLM4) using global flux fields empirically inferred from FLUXNET data. *Journal of Geophysical Research*, *116*, G02014. <https://doi.org/10.1029/2010JG001593>
- Bond, T. C., Habib, G., & Bergstrom, R. W. (2006). Limitations in the enhancement of visible light absorption due to mixing state. *Journal of Geophysical Research*, *111*, D20. <https://doi.org/10.1029/2006JD007315>
- Bonner, N. (1971). Nitrogen oxides in the stratosphere from nuclear tests: Effects on ozone concentration. Radiochem. Div., Lawrence Livermore Natl. Lab., Livermore. 4pp. (internal memo).

- Bornman, J. F., Barnes, P. W., Robinson, S. A., Ballaré, C. L., Flint, S. D., & Caldwell, M. M. (2015). Solar ultraviolet radiation and ozone depletion-driven climate change: Effects on terrestrial ecosystems. *Photochemical and Photobiological Sciences*, *14*, 88–107. <https://doi.org/10.1039/C4PP90034K>
- Boucher, N., Prézelin, B. B., Evens, T., Jovine, R., Kroon, B., Moline, M. A., & Schofield, O. (1994). Icecolors '93: Biological weighting function for the ultraviolet inhibition of carbon fixation in a natural Antarctic phytoplankton community. *Antarctic Journal of the United States*, *29*(5), 272–274.
- Bouillon, R., Eisman, J., Garabedian, M., Holick, M. F., Kleinschmidt, J., Suda, T., et al. (2006). Action spectrum for the production of previtamin D3 in human skin. *International Commission on Illumination*. technical report 174.
- Brasseur, G. P., & Solomon, S. (2005). *Aeronomy of the middle atmosphere* (3rd ed.): Springer. <https://doi.org/10.1007/1-4020-3824-0>
- Chabrilat, S., & Kockarts, G. (1997). Simple parameterization of the absorption of the solar Lyman-alpha line. *Geophysical Research Letters*, *24*, 2659–2662. <https://doi.org/10.1029/97GL52690>
- Chabrilat, S., & Kockarts, G. (1998). Correction to “Simple parameterization of the absorption of the solar Lyman-alpha line”. *Geophysical Research Letters*, *25*(1), 79. <https://doi.org/10.1029/97GL03569>
- Chang, J. S., Duewer, W. H., & Wuebbles, D. J. (1979). The atmospheric nuclear test of the 1950s and 1960s: A possible test of ozone depletion theories. *Journal of Geophysical Research*, *84*, 1755–1765. <https://doi.org/10.1029/JC084iC04p01755>
- Chang, J. S., & Wuebbles, D. J. (1984). Nuclear Explosions and Atmospheric Ozone. In J. London, & G. F. White (Eds.), *The Environmental Effects of Nuclear War, AAAS Selected Symposium* (Vol. 98, pp. 79–95): Westview Press, Inc.
- Commission Internationale de l'Éclairage (2006). *Photocarcinogenesis action spectrum (Non-Melanoma skin cancers)*: CIE S 019/E.
- Coupe, J., Bardeen, C. G., Robock, A., & Toon, O. B. (2019). Nuclear winter responses to nuclear war between the United States and Russia in the whole atmosphere community climate model version 4 and the Goddard Institute for Space Studies ModelE. *Journal of Geophysical Research*, *124*, 8522–8543. <https://doi.org/10.1029/2019JD030509>
- Coupe, J., Stevenson, S., Lovenduski, N. S., Rohr, T., Harrison, C. S., Robock, A., et al. (2021). Nuclear Niño response observed in simulations of nuclear war scenarios. *Communications Earth & Environment*, *2*. <https://doi.org/10.1038/s43247-020-00088-1>
- Covey, C., Schneider, S. H., & Thompson, S. L. (1984). Global atmospheric effects of massive smoke injections from a nuclear war: Results from general circulation model simulations. *Nature*, *308*, 21–25. <https://doi.org/10.1038/308021a0>
- Crutzen, P. J. (1970). The influence of nitrogen oxide on the atmospheric ozone content. *Quarterly Journal of the Royal Meteorological Society*, *96*, 320–325. <https://doi.org/10.1002/qj.49709640815>
- Crutzen, P. J., & Birks, J. W. (1982). The atmosphere after a nuclear war: Twilight at noon. *Ambio*, *XI*, 114–125.
- Danabasoglu, G., Bates, S. C., Briegleb, B. P., Jayne, S. R., Jochum, M., Large, W. G., et al. (2012). The CCSM4 ocean component. *Journal of Climate*, *25*, 1361–1389. <https://doi.org/10.1175/JCLI-D-11-00091.1>
- de Groot, F. R., & Van der Leun, J. C. (1994). Estimate of the wavelength dependency of ultraviolet carcinogenesis in humans and its relevance to the risk assessment of a stratospheric ozone depletion. *Health Physics*, *67*, 319–325. <https://doi.org/10.1097/00004032-199410000-00001>
- De Tommasi, E. D., Congestri, R., Dardano, P., Chiara De Luca, A., Managò, S., Rea, I., & De Stefano, M. (2018). UV-shielding and wavelength conversion by centric diatom nanopatterned frustules. *Scientific Reports*, *8*, 16285. <https://doi.org/10.1038/s41598-018-34651-w>
- Embersson, L. D., Pleijel, H., Ainsworth, E. A., van den Berg, M., Ren, W., Osborne, S., et al. (2018). Ozone effects on crops and consideration in crop models. *European Journal of Agronomy*, *100*, 19–34. <https://doi.org/10.1016/j.eja.2018.06.002>
- Flint, S. D., & Caldwell, M. M. (2003). A biological spectral weighting function for ozone depletion research with higher plants. *Physiologia Plantarum*, *117*, 137–144. <https://doi.org/10.1034/j.1399-3054.2003.1170117.x>
- Foley, H. M., & Ruderman, M. A. (1973). Stratospheric NO production from past nuclear explosions. *Journal of Geophysical Research*, *78*, 4441–4450. <https://doi.org/10.1029/JC078i021p04441>
- Forrest, K. Y. Z., & Stuhldreher, W. L. (2011). Prevalence and correlates of vitamin D deficiency in US adults. *Nutrition Research*, *31*(1), 48–54. <https://doi.org/10.1016/j.nutres.2010.12.001>
- Froidevaux, L., Kinnison, D. E., Wang, R., Anderson, J., & Fuller, R. A. (2019). Evaluation of CESM1 (WACCM) free-running and specified-dynamics atmospheric composition simulations using global multi-species satellite data records. *Atmospheric Chemistry and Physics*, *19*, 4783–4821. <https://doi.org/10.5194/acp-19-4783-2019>
- Gettelman, A., Mills, M. J., Kinnison, D. E., Garcia, R. R., Smith, A. K., Marsh, D. R., et al. (2019). The whole atmosphere community Climate Model Version 6 (WACCM6). *Journal of Geophysical Research*, *124*, 12380–12403. <https://doi.org/10.1029/2019JD030943>
- Glasstone, S., & Dolan, P. J. (1977). *The effects of nuclear weapons* (Third edition). <https://doi.org/10.2172/6852629>
- Gorshelev, V., Serdyuchenko, A., Weber, M., Chehade, W., & Burrows, J. P. (2014). High spectral resolution ozone absorption cross-sections—Part 1: Measurements, data analysis and comparison with previous measurements around 293 K. *Atmospheric Measurement Techniques*, *7*, 609–624. <https://doi.org/10.5194/amt-7-609-2014>
- Hakala-Yatkin, M., Mäntysaari, M., Mattila, H., & Tyystjärvi, E. (2010). Contributions of visible and ultraviolet parts of sunlight to photoinhibition. *Plant and Cell Physiology*, *51*, 1745–1753. <https://doi.org/10.1093/pcp/pcq133>
- Harwell, M. A., & Hutchinson, T. C. (1986). *Environmental consequences of nuclear war Volume II: Ecological and agricultural effects*. (SCOPE; 28). New York: John Wiley & Sons Ltd.
- Hurrell, J. W., Holland, M. M., Gent, P. R., Ghan, S., Kay, J. E., Kushner, P. J., et al. (2013). The community earth system model: A framework for collaborative research. *The Bulletin of the American Meteorological Society*, *94*, 1339–1360. <https://doi.org/10.1175/BAMS-D-12-00121.1>
- Iacono, M. J., Mlawer, E. J., Clough, S. A., & Morcrette, J.-J. (2000). Impact of an improved longwave radiation model, RRTM, on the energy budget and thermodynamic properties of the NCAR community climate mode. CCM3. *Journal of Geophysical Research*, *105*, 14873–14890. <https://doi.org/10.1029/2000JD900091>
- Jägermeyr, J., Robock, A., Elliot, J., Müller, C., Xia, L., Khabarov, N., et al. (2020). A regional nuclear conflict would compromise global food security. *Proceedings of the National Academy of Sciences of the United States of America*, *117*, 7071–7081. <https://doi.org/10.1073/pnas.1919049117>
- Jeffrey, S. W., MacTavish, H. S., Dunlap, W. C., Vask, M., & Groenwoud, K. (1999). Occurrence of UVA- and UVB-absorbing compounds in 152 species (206 strains) of marine microalgae. *Marine Ecology Progress Series*, *189*, 35–51. <https://doi.org/10.3354/meps189035>
- Kao, C. Y. J., Glatzmaier, G. A., Malone, R. C., & Turco, R. P. (1990). Global 3-dimensional simulations of ozone depletion under postwar conditions. *Journal of Geophysical Research*, *95*, 22495–22512. <https://doi.org/10.1029/JD095iD13p22495>
- Kataria, S., Jajoo, A., & Guruprasad, K. N. (2014). Impact of increasing Ultraviolet-B (UV-B) radiation on photosynthetic processes. *Journal of Photochemistry and Photobiology B*, *137*, 55–66. <https://doi.org/10.1016/j.jphotobiol.2014.02.004>

- Kinnison, D. E., Brasseur, G. P., Walters, S., Garcia, R. R., Sassi, F., Boville, B. A., et al. (2007). Sensitivity of chemical tracers to meteorological parameters in the MOZART-3 chemical transport model. *Journal of Geophysical Research*, D20302. 112. <https://doi.org/10.1029/2006JD007879>
- Knox, J. B. (1983). Proceedings of the Third International Conference on Nuclear War, Erice, Sicily, Italy (Laboratori Nazionali di Frascati dell' INFN); Lawrence Livermore National Laboratory Report (UCRL-89907).
- Koppers, G. A. A., & Murtagh, D. P. (1996). Model studies of the influence of O<sub>2</sub> photodissociation parameterizations in the Schumann-Runge bands on ozone related photolysis in the upper atmosphere. *Annales Geophysicae*, 14, 68–79. <https://doi.org/10.1007/s00585-996-0068-9>
- Kristensen, H. M., & Korda, M. (2020a). Russian nuclear forces, 2020. *Bulletin of the Atomic Scientists*, 76, 102–117. <https://doi.org/10.1080/00963402.2020.1728985>
- Kristensen, H. M., & Korda, M. (2020b). United States nuclear forces, 2020. *Bulletin of the Atomic Scientists*, 76, 46–60. <https://doi.org/10.1080/00963402.2019.1701286>
- Krizek, D. T. (2004). Influence of PAR and UV-A in determining plant sensitivity and photomorphogenic responses to UV-B radiation. *Photochemistry and Photobiology*, 79, 307–325. <https://doi.org/10.1111/j.1751-1097.2004.tb00013.x>
- Lewis, K. N. (1979). The prompt and delayed effects of nuclear war. *Scientific American*, 241, 35–47. <https://doi.org/10.1038/scientificamerican0779-35>
- Lindsay, K., Bonan, G. B., Doney, S. C., Hoffman, F. M., Lawrence, D. M., Long, M. C., et al. (2014). Preindustrial-control and twentieth-century carbon cycle experiments with the Earth System Model CESM1(BGC). *Journal of Climate*, 27, 8981–9005. <https://doi.org/10.1175/JCLI-D-12-00565.1>
- Llabrés, M., Agusti, S., Fernández, M., Canepa, A., Maurin, F., Vidal, F., & Duarte, C. M. (2013). Impact of elevated UVB radiation on marine biota: A meta-analysis. *Global Ecology and Biogeography*, 22, 131–144. <https://doi.org/10.1111/j.1466-8238.2012.00784.x>
- Lombardozi, D., Levis, S., Bonan, G., Hess, P. G., & Sparks, J. P. (2015). The influence of chronic ozone exposure on global carbon and water cycles. *Journal of Climate*, 28, 292–305. <https://doi.org/10.1175/JCLI-D-14-00223.1>
- Lombardozi, D., Sparks, J. P., & Bonan, G. (2013). Integrating O<sub>3</sub> influences on terrestrial processes: Photosynthetic and stomatal response data available for regional and global modeling. *Biogeosciences*, 10, 6815–6831. <https://doi.org/10.5194/bg-10-6815-2013>
- Lombardozi, D., Sparks, J. P., Bonan, G., & Levis, S. (2012). Ozone exposure causes a decoupling of conductance and photosynthesis: Implications for the Ball-Berry stomatal conductance model. *Oecologia*, 169, 651–659. <https://doi.org/10.1007/s00442-011-2242-3>
- Lovenduski, N. S., Harrison, C. S., Olivarez, H., Bardeen, C. G., Toon, O. B., Coupe, J., et al. (2020). The potential impact of nuclear conflict on ocean acidification. *Geophysical Research Letters*, 47, e2019GL086246. <https://doi.org/10.1029/2019GL086246>
- MacKie, R. M. (2000). Effects of ultraviolet radiation on human health. *Radiation Protection Dosimetry*, 91, 15–18. <https://doi.org/10.1093/oxfordjournals.rpd.a033186>
- Madronich, S., & Flocke, S. (1997). Theoretical estimation of biologically effective UV radiation at the Earth's surface. In C. Zerefos (Ed.), *Solar ultraviolet radiation modeling, measurements and effects*. NATO ASI Ser (Vol. 152, pp. 23–48): Springer. [https://doi.org/10.1007/978-3-662-03375-3\\_3](https://doi.org/10.1007/978-3-662-03375-3_3)
- Marsh, D. R., Mills, M. J., Kinnison, D. E., Calvo, J.-F., Lamarquem N., Polvani, L. M., & Polvani, L. M. (2013). Climate change from 1850 to 2005 simulated in CESM1(WACCM). *Journal of Climate*, 26, 7372–7391. <https://doi.org/10.1175/JCLI-D-12-00558.1>
- Mills, M. J., Toon, O. B., Lee-Taylor, J., & Robock, A. (2014). Multidecadal global cooling and unprecedented ozone loss following a regional nuclear conflict. *Earth's Future*, 2, 161–176. <https://doi.org/10.1002/2013EF000205>
- Mills, M. J., Toon, O. B., Turco, R. P., Kinnison, D. E., & Garcia, R. R. (2008). Massive global ozone loss predicted following regional nuclear conflict. *Proceedings of the National Academy of Sciences of the United States of America*, 105, 5307–5312. <https://doi.org/10.1073/pnas.0710058105>
- Minschwaner, K., & Siskind, D. E. (1993). A new calculation of nitric oxide photolysis in the stratosphere, mesosphere, and lower thermosphere. *Journal of Geophysical Research*, 98, 20401–20412. <https://doi.org/10.1029/93JD02007>
- Molina, M. J., Molina, L. T., Fitzpatrick, T. B., & Nghiem, P. T. (2000). In L. Möller (Ed.), *Ozone depletion and human health effects, Environmental Medicine* (pp. 28–51): Fäth & Hassler.
- National Resource Council (1985). *The effects on the atmosphere of a major nuclear exchange*: National Academy Press. <https://doi.org/10.17226/540>
- Office of Technology Assessment (1979). *The Effects of nuclear war, OTA-NS-89* (p. 151). U.S. Government Printing Office.
- Oleson, K. W., Lawrence, D. M., Bonan, G. B., Flanner, M. G., Kluzek, E., Lawrence, P. J., et al. (2010). *Technical description of version 4.0 of the Community Land Model (CLM)*. NCAR/TN-478+STR.
- Oriowo, O. M., Cullen, A. P., Chou, B. R., & Sivak, J. G. (2001). Action spectrum and recovery for in vitro UV-induced cataract using whole lenses. *Investigative Ophthalmology & Visual Science*, 42, 2596–2602.
- Para, R., Cadena, E., & Flores, C. (2019). Maximum UV Index records (2010–2014) in Quito (Ecuador) and its trend inferred from remote sensing data (1979–2018). *Atmosphere*, 10, 787. <https://doi.org/10.3390/atmos10120787>
- Pittock, A. B., Ackerman, T. P., Crutzen, P. J., MacCracken, M. C., Shapiro, C. S., & Turco, R. P. (1986). Environmental Consequences of Nuclear War Volume I: Physical and Atmospheric Effects. (SCOPE; 28) (Vol. 7, pp. 100–100) New York: John Wiley & Sons Ltd. <https://doi.org/10.1002/joc.3370070112>
- Polvani, L. M., Abalos, M., Garcia, R., Kinnison, D. E., & Randel, W. J. (2017). Significant weakening of Brewer-Dobson circulation trend over the 21st century as a consequence of the Montreal Protocol. *Geophysical Research Letters*, 45, 401–409. <https://doi.org/10.1002/2017GL075345>
- Ragni, M., Airs, R. L., Leonardos, N., & Geider, R. J. (2008). Photoinhibition of PSII in *emiliania huxleyi* (haptophyta) under high light stress: The roles of photoacclimation, photoprotection, and photorepair. *Journal of Phycology*, 44, 670–683. <https://doi.org/10.1111/j.1529-8817.2008.00524.x>
- Randel, W. J., Polvani, L., Wu, F., Kinnison, D. E., Zou, C.-Z., & Mears, C. (2017). Troposphere-stratosphere temperature trends derived from satellite data compared with ensemble simulations from WACCM. *Journal of Geophysical Research*, 122, 9651–9667. <https://doi.org/10.1002/2017JD027158>
- Robock, A. (2002). The Climatic Aftermath. *Science*, 295, 1242–1244. <https://doi.org/10.1126/science.1069903>
- Robock, A., Oman, L., & Stenchikov, G. L. (2007a). Nuclear winter revisited with a modern climate model and current nuclear arsenals: Still catastrophic consequences. *Journal of Geophysical Research*, 112, D13107. <https://doi.org/10.1029/2006JD008235>
- Robock, A., Oman, L., Stenchikov, G. L., Toon, O. B., Bardeen, C., & Turco, R. P. (2007b). Climatic consequences of regional nuclear conflicts. *Atmospheric Chemistry and Physics*, 7, 2003–2012. <https://doi.org/10.5194/acp-7-2003-2007>

- Sample, A., & He, Y.-H. (2018). Mechanisms and prevention of UV-induced melanoma. *Photodermatology, Photoimmunology & Photomedicine*, *34*, 13–24. <https://doi.org/10.1111/phpp.12329>
- Schauberger, B., Rolinski, S., Schaphoff, S., & Müller, C. (2019). Global historical soybean and wheat yield loss estimates from ozone pollution considering water and temperature as modifying effects. *Agricultural and Forest Meteorology*, *265*, 1–15. <https://doi.org/10.1016/j.agrformet.2018.11.004>
- Scherrer, K. J. N., Harrison, C. S., Heneghan, R. F., Galbraith, E., Bardeen, C. G., Coupe, J., et al. (2020). Marine wild-capture fisheries after nuclear war. *Proceedings of the National Academy of Sciences of the United States of America*, *117*, 29748–29758. <https://doi.org/10.1073/pnas.2008256117>
- Searles, P. S., Flint, S. D., & Caldwell, M. M. (2001). A meta-analysis of plant field studies simulating stratospheric ozone depletion. *Oecologia*, *127*, 1–10. <https://doi.org/10.1007/s004420000592>
- Setlow, R. B. (1974). The wavelengths in sunlight effective in producing skin cancer: A theoretical analysis. *Proceedings of the National Academy of Sciences of the United States of America*, *71*, 3363–3366. <https://doi.org/10.1073/pnas.71.9.3363>
- Solomon, S., Ivy, D. J., Kinnison, D. E., Mills, M. J., Neely, R. R., & Schmidt, A. (2016). Emergence of healing in the Antarctic ozone layer. *Science*, *353*, 269–274. <https://doi.org/10.1126/science.aae0061>
- Solomon, S., Kinnison, D., Bandoro, J., & Garcia, R. (2015). Simulation of polar ozone depletion: An update. *Journal of Geophysical Research: Atmospheres*, *120*, 7958–7974. <https://doi.org/10.1002/2015JD023365>
- Stenke, A., Hoyle, C. R., Luo, B., Rozanov, E., Gröbner, J., Maag, L., et al. (2013). Climate and chemistry effects of a regional scale nuclear conflict. *Atmospheric Chemistry and Physics*, *13*, 9713–9729. <https://doi.org/10.5194/acp-13-9713-2013>
- Stock, C. A., John, J. G., Rykaczewski, R. R., Asch, R. G., Cheung, W. L., Dunne, J. P., et al. (2017). Reconciling fisheries catch and ocean productivity. *Proceedings of the National Academy of Sciences of the United States of America*, *114*, E1441–E1449. <https://doi.org/10.1073/pnas.1610238114>
- Stone, K. A., Solomon, S., & Kinnison, D. E. (2018). On the identification of ozone recovery. *Geophysical Research Letters*, *45*, 5158–5165. <https://doi.org/10.1029/2018GL077955>
- Toon, O. B., Bardeen, C. G., Robock, A., Xia, L., Kristensen, H., McKinzie, M., et al. (2019). Rapidly expanding nuclear arsenals in Pakistan and India portend regional and global catastrophe. *Science Advances*, *10*, eaay5478. <https://doi.org/10.1126/sciadv.aay5478>
- Toon, O. B., Robock, A., & Turco, R. P. (2008). Environmental consequences of nuclear war. *Physics Today*, *61*, 37–42. <https://doi.org/10.1063/1.3047679>
- Toon, O. B., Turco, R. P., Westphal, D., Malone, R., & Liu, M. S. (1988). A multidimensional model for aerosols; Description of computational analogs. *Journal of the Atmospheric Sciences*, *54*(2), 2123–2144. [https://doi.org/10.1175/1520-0469\(1988\)045<2123:AMMFAD>2.0.CO;2](https://doi.org/10.1175/1520-0469(1988)045<2123:AMMFAD>2.0.CO;2)
- Turco, R. P., Toon, O. B., Ackerman, T. P., Pollack, J. B., & Sagan, C. (1983). Nuclear Winter: Global consequences of multiple nuclear explosions. *Science*, *222*, 1283–1292. <https://doi.org/10.1126/science.222.4630.1283>
- Wagman, B., Lundquist, K. A., Tang, Q., Glascoe, L. G., & Bader, D. C. (2020). Examining the climate effects of a regional nuclear weapons exchange using a multiscale atmospheric modeling approach. *Journal of Geophysical Research*, *125*, e2020JD033056. <https://doi.org/10.1029/2020JD033056>
- Wargent, J. J., & Jordan, B. R. (2013). From ozone depletion to agriculture: Understanding the role of UV radiation in sustainable crop production. *New Phytologist*, *197*, 1058–1076. <https://doi.org/10.1111/nph.12132>
- World Health Organization (2002). *Global solar UV Index: A practical guide*: World Health Org.
- Xia, L., Nowack, P. J., Robock, A., & Tilmes, S. (2017). Impacts of stratospheric sulfate geoengineering on tropospheric ozone. *Atmospheric Chemistry and Physics*, *17*(11), 11913–11928. <https://doi.org/10.5194/acp-17-11913-2017>
- Xu, J. L. T., Gao, K. G. S., W. Z., K., Riebessell, U., Zhao, W., Gao, K., & Riebessell, U. (2016). The role of coccoliths in protecting *Emiliania huxleyi* against stressful light and UV radiation. *Biogeosciences*, *13*, 4637–4643. <https://doi.org/10.5194/bg-13-4637-2016>
- Yu, P., Davis, S. M., Toon, O. B., Portmann, R. W., Bardeen, C. G., Barnes, J. E., et al. (2020). Persistent Stratospheric Warming Due to 2019–2020 Australian Wildfire Smoke. *Geophysical Research Letters*, *48*, e92609. <https://doi.org/10.1029/2021GL092609>
- Yu, P., Toon, O. B., Bardeen, C. G., Zhu, Y., Rosenlof, K. H., Portmann, R. W., et al. (2019). Black carbon lofts wildfire smoke high into the stratosphere to form a persistent plume. *Science*, *365*, 587–590. <https://doi.org/10.1126/science.aax1748>